DHX36 binding induces RNA structurome remolding and regulates RNA abundance via m^6A/YTHDF1

Yuwei Zhang[1,7], Jieyu Zhao[2,7], Xiaona Chen[3,4], Kaixin Lyu[2], Yiliang Ding[5], Hao Sun[1,*], Chun-Kit Kwok[2,6*], and Huating Wang[3,4*]

1 Department of Chemical Pathology, Li Ka Shing Institute of Health Sciences, Chinese University of Hong Kong, Hong Kong SAR, China.
2 Department of Chemistry and State Key Laboratory of Marine Pollution, City University of Hong Kong, Hong Kong SAR, China.
3 Department of Orthopaedics and Traumatology, Li Ka Shing Institute of Health Sciences, Chinese University of Hong Kong, Hong Kong SAR, China.
4 Center for Neuromusculoskeletal Restorative Medicine Limited, Hong Kong SAR, China.
5 Department of Cell and Developmental Biology, John Innes Centre, Norwich Research Park, Norwich NR4 7UH, U.K.
6 Shenzhen Research Institute of City University of Hong Kong, Shenzhen, China
7 These authors contribute equally to this paper as first authors.
* Co-correspondence

Address correspondence to: Huating Wang, 507A Li Ka Shing Institute of Health Sciences, Prince of Wales Hospital, Chinese University of Hong Kong, Hong Kong SAR, China. Phone: (852)3763-6047; Fax: (852)-2632-0008; E-mail: huating.wang@cuhk.edu.hk

Chun-Kit Kwok, Department of Chemistry and State Key Laboratory of Marine Pollution, City University of Hong Kong, Kowloon Tong, Hong Kong SAR, China. Phone: (852)3442-6858; Fax: (852)-3442-0522; Email: ckkwok42@cityu.edu.hk

Hao Sun, 503, Li Ka Shing Institute of Health Sciences, Prince of Wales Hospital, Chinese University of Hong Kong, Hong Kong, China. Phone: (852)3763-6048; E-mail: haosun@cuhk.edu.hk

Running title: DHX36 remodels RNA structures and regulates mRNA abundance.

Keywords: DHX36, RNA secondary structure, post-transcriptional regulation, N6-methyladenosine, YTHDF1

Conflict of interest: the authors have declared that no conflict of interest exists.

Abstract

RNA structure constitutes a new layer of gene regulatory mechanisms. RNA binding proteins can modulate RNA secondary structures, thus participating in post-transcriptional regulation. The DEAH-box helicase 36 (DHX36) is known to bind and unwind RNA G-quadruplex (rG4) structure but the transcriptome-wide RNA structure remodeling induced by DHX36 binding and the impact on RNA fate remain poorly understood. Here, we investigate the RNA structurome alteration induced by DHX36 depletion. Our findings reveal that DHX36 binding induces structure remodeling not only at the localized binding sites but also on the entire mRNA transcript most pronounced in3'UTR regions. DHX36 binding increase structural accessibility at 3'UTRs which is correlated with decreased post-transcriptional mRNA abundance. Further analyses and experiments uncover that DHX36 binding sites are enriched for N6-methyladenosine (m^6A) modification and YTHDF1 binding; and DHX36 induced structural change may facilitate YTHDF1 binding to m^6A sites leading to RNA degradation. Altogether, our findings uncover the structural remodeling effect of DHX36 binding and its impact on RNA abundance through regulating m6A dependent YTHDF1 binding.

Keywords

DHX36, RNA secondary structure, post-transcriptional regulation, N6-methyladenosine, YTHDF1

Introduction

In recent years, interest in RNA secondary structure has exploded due to its implications in almost all biological functions and its newly appreciated capacity as a therapeutic agent/target. [1]. Examples of secondary structures include long-range interactions, hairpins, R-loops and G-quadruplexes (G4) and they are formed through interactions of non-adjacent nucleotides. Due to their large size, the structures of mRNAs are challenging to study, but the past decade has seen rapid development in RNA structure-probing methods to capture transcriptome-wide RNA structures (that is, RNA structurome) in many species and across conditions [1]. For example, Structure-seq [2] was developed for mapping *in vivo* RNA structures and interactions by coupling chemical structure probing with deep sequencing. Chemical modification on the unpaired bases leads to the reverse transcription (RT) stops, which can be read out as a reactivity score and be used to infer RNA structures. It provides quantitative RNA secondary structural information across thousands of transcripts at nucleotide resolution. Several other probing methods have also been developed [3-5] thus providing tools for systematic interrogation of *in vivo* RNA structures.

The roles of RNA secondary structures in key biological functions can be seen in every type of RNAs mainly because of their importance in mediating RNA association with RNA binding proteins (RBPs) [6-9]. During the mRNA lifecycle, RBPs regulate diverse transcriptional and post-transcriptional stages. They can bind to pre-mRNA molecules in the nucleus and regulate its maturation and transportation to the cytoplasm where they regulate translation and degradation. Emerging evidence from transcriptome wide profiling of RBP binding such as crosslinking immunoprecipitation sequencing (CLIP-seq) and RNA Bind-n-Seq (RBNS) suggests that other than

RNA sequence motifs, local RNA secondary structures play a determinant role in RBP binding and regulation [10-13]. Still, the field remains largely nascent and many key questions need to be answered such as: to what degree and how RNA secondary structures contribute to RBP regulation of post-transcriptional RNA processing?

The interplay between RBPs and RNA structures is made more complex by the fact that RBP binding also orchestrates secondary structure formation and stabilization. Of note, RNA structure formation is to a large extent modulated by helicases that can bind and rearrange RNA structures and ribonucleoprotein complex, thus playing crucial roles in transcriptional, post-transcriptional and translational regulation [7, 14]. For example, DHX36 is a DEAH-Box helicase which can bind and unwind RNA G-quadruplex (rG4s) and RNA duplex via a conserved DHX36-specific motif (DSM) and other auxiliary domains [15, 16]. rG4 structures are non-canonical secondary structures formed in G-rich RNA sequences by the stacking of guanine-quartets through Hoogsteen hydrogen bonding [17]. Recent studies suggest that rG4 formation can modulate (either favor or block) *in vitro* RBP binding to mRNA molecules [18, 19]. Therefore, by unwinding rG4s, DHX36 plays an essential role in post-transcriptional regulation at many levels [15, 20-23]. For example, in our recent study [22], by CLIP-seq profiling, we found that DHX36 primarily binds with rG4s in myoblast cells and unwinding 5'UTR rG4s endows its ability to promote mRNA translation. Nevertheless, this study also revealed its binding at CDSs and 3'UTRs and introns, implying potential functions of DHX36 in regulating mRNA abundance as well as other aspects of mRNA metabolism. Apart from rG4-dependent mechanisms, an *in vitro* study based on the crystal structure of DHX36 protein revealed that DHX36 can also bind to and unwind RNA duplexes [15]. Therefore, it is imperative to

illuminate how DHX36 binding induces RNA structural changes system-wide and how the changes control post-transcriptional mRNA processing.

The RNA structure/RBP interplay becomes more intriguing by the recent discovery of the interplay between RNA structures, RNA modifications and RBP binding [13]. N6-methyladenosine (m^6A) modification is the most abundant internal modification in mRNAs and contributes to diverse fundamental cellular functions [25-28], which is largely dependent on the "reader" proteins that recognize and bind with m^6A sites [24]. Among them, YTHDF1 reader is known for regulating mRNA degradation and translation via its m^6A binding ability [25-28]. Interestingly, m^6A modification can alter the local structures in RNAs via so-called "m^6A-switch" to modulate the binding of RBPs [13, 29]. Mutually, RNA structural accessibility also orchestrates the abundance and effects of m^6A, because the binding activity of "writer" complex METTL3/METTL14 [30], "erasers" FTO and ALKBH5 [31, 32], and some "readers" [13, 29] are sensitive to target RNA structures. YTHDF readers appear to prefer unstructured RNAs [33], but it remains unclear whether unwinding of RNA structures is essential for the binding of these proteins to m^6A sites.

In this study, we investigated how DHX36 binding influences mRNA secondary structures *in vivo* and the mechanism underlying DHX36-induced structural changes in post-transcriptional regulation. By conducting the RNA Structure-seq in wild type (WT) and DHX36 knockout (DHX36-KO) HEK293T cells, we found that DHX36 depletion induces global loss of RNA structures. Combining with DHX36 binding profiles, we found that DHX36 binding increases RNA structure accessibility especially in 3'UTRs. Further analyses demonstrate that induced accessible structures in 3'UTRs is related to post-transcriptional mRNA decrease Moreover, m^6A dependent

YTHDF1 binding /events are enriched in the DHX36 binding sites and may mediate DHX36 regulation of mRNA abundance. Additional experimental assays were conducted on selected target mRNAs to substantiate that DHX36 binding promotes YTHDF1 binding to m^6A sites and subsequent mRNA degradation. Altogether, our findings uncover transcriptome-wide structural changes induced by DHX36 binding and elucidate how the changes orchestrate mRNA abundance.

Results

In vivo RNA structurome profiling unveils DHX36 depletion-induced global loss of RNA structures.

To have a thorough understanding of DHX36 function in modulating RNA structures [15], we deleted DHX36 in HEK293T cells using CRISPR/Cas9-mediated gene editing to obtain a DHX36-knockout (KO) cell line (Fig. 1A) and performed a slightly modified SHAPE-based Structure-seq [34] in WT and KO cells. 2-methylnicotinic acid imidazolide (NAI) but not dimethyl sulfide (DMS) was used therefore all four RNA bases were modified (Fig. 1B). NAI treatment can acylate the 2'hydroxyl group of all four RNA bases not involved in base pairing, thus blocking the reverse transcription (RT) at these positions and generating discriminative signals of RT stops in sequencing data (Fig. 1C). Two replicates were performed for each sample and high reproducibility was observed when correlating the RT stops of each nucleotide between the two replicates (r=0.75-0.82, Fig. S1A). After removing transcripts with low RT stop coverage, the analysis yielded 22,390 mRNAs with at least 1 RT stop per nucleotide (Supplementary Table S1). SHAPE reactivity of each nucleotide was then calculated by subtracting the number of RT stops of mock (DMSO)-treated sample from the NAI-treated sample to yield an accurate assessment of RNA accessibility (see Methods) [35]. As additional validation to the high quality of our data, the SHAPE reactivity profiles of 18S rRNA were calculated and in concordance with the phylogenetically derived structures, indicating that our data can accurately reflect *in vivo* RNA secondary structures (Fig. S1B).

Next, to examine the effect of DHX36 loss on RNA structures, an average value and a Gini

index of SHAPE reactivity scores were calculated. Higher Gini index is correlated with more heterogeneous distribution of SHAPE reactivity scores thus increased structurization of the entire mRNA [3, 36]. As shown in Fig. 1D-E, the average SHAPE reactivity scores of mRNAs were significantly decreased (FC=0.74, P<2.23e-308) in the KO vs. WT cells; a concomitant increase of Gini index (FC=1.03, P=1.81e-107) was detected, indicating DHX36 loss induces global mRNA structurization thus decreased accessibility. Further examination of the structural changes at different mRNA regions (5'UTRs, CDSs and 3'UTRs) by binned reactivity profiles across the length of each region and ΔReactivity (the reactivity scores in KO sample subtracted by that in WT sample) revealed decreased SHAPE reactivity and increased accessibility in all regions upon DHX36 loss and 3'UTRs exhibited the largest gain of accessibility (Fig. 1F). In sum, *in vivo* RNA structurome mapping provides a global view of DHX36-mediated RNA structural changes.

DHX36 binding induces RNA structural loss and gained accessibility.

To elucidate the structural changes directly induced by DHX36 binding, we next interrogated DHX36-bound mRNAs (Fig. 2A). The publicly available DHX36 photoactivatable-ribonucleoside-enhanced crosslinking and immunoprecipitation (PAR-CLIP) data from HEK293 cells [37] were re-analyzed to identify crosslinking sites at single-nucleotide resolution using the CLIP Tool Kit (CTK) [38]. A total of 4,361 crosslinking sites were identified (Supplementary Table S2), of which 4,263 were annotated to 2,886 mRNAs. Close examination revealed that DHX36 binding preferentially resided in 3'UTR regions, especially around the stop codons (Fig. 2B-C). However, 5'UTRs harbored the highest DHX36 binding density after

normalization by the region length (Fig. S2A). Further prediction showed that 79% of the DHX36 binding sites possessed potential rG4s of various subtypes with the highest enrichment and stability found at the 5'UTRs (Fig. 2D, Fig. S2B-C, Supplementary Table S2), confirming that indeed rG4 structure is the predominant RNA substrate for DHX36 binding [22] This was further validated by the results from *in vitro* RBNS in which we incubated the His-tagged RHAU53 peptide of DHX36 protein with a 40-nt random RNA library in the presence of either K^+, which stabilizes rG4 folding, or Li^+, which destabilizes rG4 folding. As expected, the RHAU53-bound RNAs were biased towards G-repeat 6mer motifs (Fig. S2D) and were enriched for potential rG4s (Fig. S2E) in the presence of K^+. The highest enrichment of K^+ RBNS motifs was detected in 5'UTR binding sites supporting the preferred binding of DHX36 to rG4s in 5'UTRs (Fig. S2F).

Further analysis uncovered that the above defined DHX36-bound mRNAs showed significantly decreased reactivity scores (FC=0.68, *P*=1.66e-238) and increased Gini index (FC=1.05, *P*=7.14e-80) in KO cells compared to WT (Fig. 2E), suggesting DHX36 binding induces mRNA structural loss thus increases structural accessibility. Compared to unbound mRNAs, DHX36-bound mRNAs displayed larger loss in reactivity (*P*=4.56e-53) and gain in Gini index (*P*=5.22e-28) in KO vs. WT cells (Fig. 2F), confirming that indeed direct DHX36 binding induces structural loss. Further analyses of each transcript region revealed that 3'UTRs exhibited the largest structural gain upon DHX36 loss, followed by CDSs and 5'UTRs (Fig. 2G-H, Fig. S3A). To investigate whether the structural gain towards the 3'end is driven by innate sequence features, we correlated the regional reactivity change with GC-content or sequence length of the designated region and found the large structural change of 3'UTRs is probably caused by low GC content (r=0.312, *P*=8.40e-113; Fig. 2I,

Fig. S3B-D).

Since the above comparison of average SHAPE reactivity or Gini index cannot pinpoint the exact structural changing sites across the entire mRNA, we next employed dStruct [39] to uncover differentially reactive regions (DRRs). As a result, a total of 50,683 DRRs were identified from 2,419 DHX36-bound mRNAs; and only 3,564 possessed DHX36 binding sites (Fig. 2J, Supplementary Table S3), indicating DHX36 binding leads to structural alterations at both localized binding sites and also distal sites without direct binding. Furthermore, DHX36 loss mainly led to structural gain of DRRs, with 74% of DRRs exhibiting decreased average SHAPE reactivity while 26% increased (Fig. S3E). Metagene analysis revealed that DRRs preferentially resided in 3'UTRs, followed by CDSs and 5'UTRs (Fig. 2K). Upon normalization by the number of regional binding events, we found that 3'UTRs were most enriched for DRRs (Fig. S3F), indicating that DRRs were not evenly distributed among the binding sites.

The discrepancy between the preferential binding of DHX36 to 5'UTRs (Fig. S1C) and the enrichment of DRRs within 3'UTRs (Fig. S3F) led us speculate that DHX36 binding in different regions may not confer the same structural modifying effect. To test this notion, we selected the mRNAs with exclusive DHX36 binding in only one region, 3'UTRs or CDSs or 5'UTRs to compare the DRR distribution. We found that DRRs were enriched towards the end of CDSs or 3'UTRs with limited dependence on DHX36 binding location (Fig. 2L). Consistently, binding events located in any transcript region induced higher changes of SHAPE reactivity and Gini index in 3'UTRs but exerted limited effect on 5'UTRs (Fig. S3G-I). For example, DHX36 binding to the 5'UTR of mRNA PYCR1 and the 3'UTR of CCNA2 both led to the highest reactivity increase and structural

loss in their 3'UTRs (Fig. 2M).

DHX36 induces localized structural loss in 3'UTRs binding sites

After dissecting the structural changes at whole-transcript and regional scale, we further examined more localized structural effects surrounding DHX36 binding sites (+/- 50nt of the crosslink site). As expected, SHAPE reactivity at the DHX36 binding sites dramatically decreased in KO vs. WT cells (Fig. 3A), supporting that DHX36 loss induces local structural gain and reduces accessibility. Given that SHAPE reactivity only provides probabilistic inference of RNA secondary structures but cannot be used to distinguish paired from single-stranded bases, we then calculated the base-pairing probability (BPP) constrained by SHAPE reactivity. Consistently, higher BPPs were observed in KO cells, further confirming the reduced structural accessibility upon DHX36 loss (Fig. 3A). Next, we examined the DRR distribution within DHX36 binding sites and found 71.69% of the binding sites possessed DRRs (Fig. 3B, Supplementary Table S3). Five bins were generated for each DRR and lower reactivity was detected in KO cells (Fig. S4A), indicating that most DRRs gained in structures upon DHX36 loss. Altogether, the above results suggest that DHX36 binding induces structural loss at the binding site, which is in line with its known helicase unwinding function. Interestingly, closer examination uncovered similar proportion and subtypes of rG4s between DRR-containing (Fig. 3C, 78%) and all DHX36 binding sites (Fig. 2D, 79%), suggesting that DHX36 did not discriminately unwind rG4s; this was also supported by similar distribution of reactivity scores and BPPs between rG4-containing and non-rG4 sites (Fig. 3D, Fig. S4B).

To further interrogate localized structural changes at different mRNA regions, we classified the DHX36 binding sites by regions and separately profiled reactivity and BPPs. Of note, the largest decrease in SHAPE reactivity (Fig. 3E) and increase in BPP (Fig. S4C) upon DHX36 loss was observed in the 3'UTR binding sites. Moreover, more than a half of DRRs were located within 3'UTR regions (Fig. 3F). Furthermore, after normalization by the total number of binding sites in each region, DRRs were most enriched in the 3'UTR binding sites (Fig. S4D), indicating 3'UTRs undergo the largest structural change upon DHX36 binding. The structure folding predicted by ViennaRNA package [40] using SHAPE reactivity as constraint further illustrated extensive structure rearrangement in the 3'UTRs. For example, DHX36 loss resulted in less accessible structure at the binding site within the 3'UTR of *JUN* mRNA (Fig. 3G-H).

Next, to investigate why 3'UTR binding sites harbored the highest structural increase upon DHX36 loss, we speculated that it may be related to high GC contents since GC base pairs are more stable than AU base pairs thus more resistant to DHX36 unwinding [41]. Alternatively, this could be caused by the relatively high average sequence length of 3'UTRs compared to 5'UTRs and CDSs (Fig. S3C) [42, 43]. To test this, we established multivariable linear regression models, in which the localized reactivity changes of all DHX36 binding sites or those located in 5'UTRs, CDSs or 3'UTRs was each used as the response variable. The GC content of the DHX36-bound region (Fig. S3B), the localized GC content of the 100nt DHX36 binding site (Fig. S4E) and the length of the bound region were not collinear to each other (Supplementary Table S4) thus used as the explanatory variables. In the model based on all DHX36 binding sites (Fig. 3I, top row), we found that low GC contents of the entire transcript regions (regional GC contents), where DHX36 binding sites reside,

to a large extent explained the highest localized structural changes of 3'UTR binding sites, while the GC contents of localized binding sites (localized GC contents) and the length of the transcript regions conferred limited contribution. Notably, the above phenomenon was not observed in the models for binding sites in individual mRNA regions (the last three rows of Fig. 3I), suggesting that differential regional GC contents impact the unwinding effect of DHX36. In addition, the limited contribution of localized GC contents to structural changes indicated that DHX36 binding exerted discriminative unwinding power in the susceptible contexts (i.e. 3'UTRs with low regional GC contents).

DHX36 binding-induced structurome remodeling effect is conserved in C2C12 myoblast cells.

To examine whether the effect of DHX36 binding on RNA structure remodeling is conserved in other cell types, we next conducted Structure-seq with DMS in our previously established WT and Dhx36-KO C2C12 mouse myoblast cell lines [22]. The good correlation of the identified RT stops between the two replicates and the concordance between reactivity score as well as the phylogenetically derived 18S rRNA structures demonstrated the high quality of our data (Fig. S5A-B). As a result, a total of 25,637 mRNAs were identified with sufficient RT coverage (Supplementary Table S5). Integrating our published DHX36 CLIP-seq from C2C12 cells [22], similar analysis was performed to define DHX36 binding induced RNA structural changes. Both DMS reactivity and Gini index indicated that DHX36 loss induced significant structural loss in DHX36-bound mRNAs especially at 3'UTRs (Fig. S5C-E), resembling the findings from HEK293T cells (Fig. 2G-H). Next, we took a closer view of the localized structural changes at different mRNA

regions and also detected the most pronounced changes at the DHX36-binding sites within 3'UTRs (Fig. S5F). Altogether, the above findings demonstrate that DHX36 binding induced structural loss may be a conserved phenomenon in various cells, which triggered us to further elucidate the functional consequences.

DHX36 induced 3'UTR structural change is associated with post-transcriptional regulation of mRNA abundance

Secondary structural change within 3'UTRs is an emerging mechanism in post-transcriptional regulation of mRNA abundance via modulating RNA stability or degradation [12, 44-46]. To examine whether the DHX36 induced 3'UTR structural changes are associated with RNA abundance, we took advantage of the existing RNA-seq data generated from whole-cell RNAs or chromatin-associated RNAs in WT or DHX36 KO HEK293 cells [37] and calculated the RNA abundance fold change (FC) in whole cell and chromatin fraction respectively; a post-transcriptional FC (pFC) index was then deduced by dividing the chromatin by the whole cell FC (Fig. 4A). With a threshold of pFC > 1.5, 1998 genes were identified as post-transcriptionally down-regulated (pDGs) upon DHX36 loss and 1850 up-regulated genes (pUGs) (Fig. 4B). Furthermore,149 (7.5%) pDGs and 517 (27.9%) pUGs bound by DHX36 were defined as DHX36 post-transcriptional regulatory targets (*P*=6.43e-63; Fig. 4C, Supplementary Table S6). These target genes displayed higher pFCs compared to all protein-coding genes, (*P*=2.58e-36, Fig. 4D), indicating that DHX36 loss leads to a post-transcriptional increase and DHX36 binding is indeed associated with post-transcriptional regulation of mRNA abundance. Next, we correlated the structural changes of the target mRNAs

with the abundance changes and uncovered that the pUG targets showed higher reactivity loss thus structural gain compared with the pDGs (*P*=6.04e-10; Fig. 4E), suggesting that DHX36 binding-induced structural loss is associated with post-transcriptional down-regulation of mRNA abundance. Next, we calculated the correlation of the fold change of average reactivity of the entire transcript with pFCs and found that reactivity changes were inversely correlated with RNA abundance changes (Fig. 4F). When each transcript region was examined, an inverse correlation was also observed (Fig. 4G-I); compared to 5'UTRs and CDSs which showed modest correlation (r=-0.05, *P*=0.001 for 5'UTRs; r=-0.06, *P*=1.35e-06 for CDSs; Fig. 4G-H), a higher correlation was observed between the structural gain in 3'UTRs and the mRNA abundance increase (r=-0.18, *P*=2.75e-39; Fig. 4I), suggesting that 3'UTR structures may exert dominant contribution in post-transcriptional regulation of mRNA abundance.

In addition, we compared the localized structural changes of pUG and pDG targets and found that pUGs showed higher reactivity loss thus structural gain than pDGs upon DHX36 inactivation (Fig. 4J). Moreover, the most overwhelming localized structural increase of pUGs was observed in 3'UTR binding sites (Fig. 4K). Altogether the above findings suggest that DHX36 binding-induced 3'UTR structural decrease is associated with post-transcriptional down-regulation of mRNA abundance.

DHX36-induced RNA structural accessibility facilitates m^6A dependent YTDHF1 binding and RNA degradation.

To further fathom the underlying mechanism of how DHX36 binding regulates mRNA abundance via structural modulation, we realized that the enrichment of DHX36 binding sites within 3'UTRs especially around stop codons was reminiscent of the distribution of m^6A modification [47] and YTHDF1 binding [48]. Moreover, it has been reported that potential rG4s co-localize with m^6A sites [49, 50] and YTHDF1 can regulate mRNA degradation in HEK293 cells [25, 26], triggering us to speculate that DHX36 effect on mRNA abundance may be mediated by m^6A/YTHDF1 (Fig. 5A). To test the above hypothesis, we leveraged the available miCLIP data [47] and iCLIP data for YTHDF1 [48] to identify m^6A and YTHDF1 binding within the DHX36 3'UTR binding sites. As a result, these sites were significantly enriched for canonical m^6A and YTHDF1 binding motifs (Fig. S6A, Fig. 5B). Furthermore, approximately 20% of these 3'UTR DHX36 binding sites overlapped with m^6A and 24% with YTHDF1 binding, which significantly overwhelmed the overlapping with randomly selected sites (P<0.01, Fig. 5C-D; Supplementary Table S7). Altogether, the above results demonstrate that DHX36 binding co-localizes with m^6A/YTHDF1 within 3UTRs.

Next, to investigate whether the co-binding is associated with DHX36 regulation of post-transcriptional RNA abundance, we found DHX36-bound mRNAs with m^6A/YTHDF1 within their 3'UTRs showed significantly higher pFCs, compared to those without m^6A/YTHDF1 (P=5.46e-22, Fig. 5E). To further elucidate whether YTHDF1 regulates RNA degradation, we harnessed the available 4-thiouridine labeling (4SU-TT-seq) data generated from WT and YTHDF1-KO HEK293 cells [25]. 4SU-TT-seq infers mRNA half-life through estimating the fraction of 4SU-labelled nascent RNAs in total RNA pool. A total of 3738 mRNAs showed prolonged half-life (KO/WT>1) upon YTHDF1 loss thus defined as YTHDF1 degradation targets. Among the

327 pUG targets with DHX36 binding at their 3'UTRs, 157 were significantly overlapped with these YTHDF1 degradation targets and defined as DHX36/m^{6}A/YTHDF1 degradation targets (*P*=0.004, Fig. 5F); but no significant overlapping was observed for pDG targets (*P*=0.445, Fig. S6B). The above results suggest that YTHDF1 co-binding with DHX36 leads to mRNA degradation. Furthermore, significant overlapping between 3'UTR YTHDF1-binding sites and DRR-containing DHX36 binding sites within 3'UTRs (*P*=1.81e-12, Fig. 5G) was also detected, suggesting a possibility that DHX36 binding-induced 3'UTR structural accessibility may facilitate YTHDF1 binding. As YTHDF1 binding activity can be influenced by both m^{6}A level [51] and substrate structure [33], we tested if DHX36 loss leads to reduced m^{6}A level which was inferred by probing the structural signature at the m^{6}A site according to the m^{6}A switch theory [3]. The m^{6}A-induced signature structural decrease was observed in both WT and DHX36-KO cells (Fig. S6C). Moreover, a similar structural decrease pattern at the m^{6}A sites located within DHX36 binding sites was detected in both WT and DHX36-KO cells (Fig. 5H), demonstrating that DHX36 inactivation exerted limited influence on the m^{6}A level. This leads us to speculate that DHX36 binding-induced structural accessibility may expose m^{6}A sites to facilitate YTHDF1 binding and subsequent mRNA degradation.

DHX36 facilitates YTHDF1 binding to decrease mRNA stability on selected targets

To further test the above notion, we selected four representative mRNAs including EZR (ENST00000367075), MEPCE (ENST00000310512), PHF23 (ENST00000320316) and ZNF768 (ENST00000380412) from the DHX36/m^{6}A/YTHDF1 degradation target list and performed

additional experimental validation in HEK293T cells. The abundance of these mRNAs was increased in whole cell but not chromatin faction upon DHX36 loss (Fig. 6A). A DHX36 binding site was identified within the 3'UTR of each target, and this site was also co-bound by m^6A/YTHDF1. The SHAPE reactivity and structural accessibility of these sites showed significant decrease upon DHX36 inactivation (Fig. 6B). First, the decreased levels of these mRNAs in DHX36 KO vs. WT were confirmed by RT-qPCR (Fig. 6C). When the cells were treated with actinomycin D for 4 or 8 hrs, all four mRNAs showed increased RNA stability and decreased degradation rate in the DHX36-KO vs. WT cells (Fig. 6D), confirming that DHX36 regulates the degradation of these mRNAs. As expected, the calculated half-life of these mRNAs with the 4SU-TT-seq data [52] were significantly increased upon YTHDF1 inactivation (Fig. 6E). To further examine whether YTHDF1 binding to m^6A was facilitated by DHX36 binding, we conducted YTHDF1 RNA immunoprecipitation (RIP) (Fig. 6F) and found YTHDF1 binding to all four mRNAs was significantly impaired in DHX36-KO vs. WT cells (Fig. 6G); and the decreased interaction was not due to reduced YTHDF1 expression (Fig. 6H). Altogether, the above results validate that DHX36 binding induced structural accessibility in 3'UTRs enhances m^6A dependent YTHDF1 binding to promote target mRNA degradation (Fig. 7).

Discussion

In this study, we elucidated DHX36 orchestrated RNA structural remodeling and how it controls post-transcriptional RNA abundance. Harnessing *in vivo* RNA Structure-seq we probed transcriptomic structural changes induced by DHX36 loss. Combining with DHX36 binding profiles, we uncovered that DHX36 binding induces structural loss thus increased RNA accessibility especially in 3'UTR regions. Moreover, we discovered that the DHX36-induced 3'UTR structural changes are associated with post-transcriptional regulation of RNA abundance through modulating YTHDF1 binding to m^6A sites.

Our study provides the very first view of how DHX36 modulates global RNA structures. DHX36 is best known for its G4 binding and unwinding ability. Transcriptome-wide binding profiling has been reported by us and several other groups to show it predominant binding on rG4s especially within 5'UTR regions [22, 37, 53]. The unwinding effect of DHX36 binding on target rG4s has also been characterized extensively [21, 22, 54-56]. In these studies, *in vivo* DHX36-induced structural changes were quantified by either indirect measurement (using rG4-specific chemical ligand or antibody) or disrupting rG4 forming sequences, but neither provides enough resolution for a closer look into DHX36 binding sites and disrupting rG4 forming sequences is also low-throughput. Moreover, despite rG4 being the dominant structure substrates for DHX36, it can also bind with other structure elements such as RNA duplexes [15]. Therefore, the Structure-seq allowed us to interrogate *in vivo* transcriptomic structure remodeling induced by DHX36. The high resolution enabled us to precisely pinpoint the structure changing sites. It is interesting to find out that DHX36 binding causes the largest structural decrease within 3'UTRs followed by CDSs and

5’UTRs (Fig. 2G), and the structure remodeling effect was conserved in both human HEK293T and mouse C2C12 cells (Fig. 2; Fig. S5). More intriguingly, DHX36 binding-induced structure remodeling was not confined to localized binding sites (Fig. 2J) but extended across the entire transcript especially in 3’UTRs (Fig. 2K-L). This phenomenon is reminiscent of the structure remodeling effect of some other RBPs such as PUM2 [57] and Dbp1 [58], whose modulation also triggers structural changes on both RBP-bound and unbound sites especially those in 3’UTRs. This also highlight the need to consider both localized and entire transcript level changes when examining RNA structure contribution to post-transcriptional regulation.

Our study also uncovers a previously uncharacterized mechanism through which DHX36 regulates mRNA abundance. We demonstrated that DHX36 binding-induced structural accessibility of 3’UTRs is involved in post-transcriptional regulation of RNA abundance (Fig. 4I). The co-localization of DHX36 binding sites with m^6A modification and YTHDF1 binding (Fig. 5B-D) especially around stop codons (Fig. 2C) inspired our mechanistic investigation of the role of m^6A/YTHDF1 in mediating DHX36 effect on RNA degradation. Of note, Youn et.al detected subcellular co-localization of DHX36 and YTHDF1 in stress granule using *in vivo* proximity-dependent biotinylation analysis in HEK293 cell [59], further supporting the potential synergistic action between these two RBPs. DHX36 binding appears to exert limited influence on m^6A deposition (Fig. 5H), suggesting that the inhibited YTHDF1 activity upon DHX36 loss is not caused by reduced m^6A deposition. The known preference of YTH domain towards less structured RNAs [33] led us to believe that DHX36 induced structural accessibility facilitates YTHDF1 recruitment to m^6A sites. This was further validated by additional assays conducted on selected

targets including EZR, MEPCE, PHF23, and ZNF768 (Fig. 6). Therefore, our findings suggest a previously unknown mechanism that DHX36 binding-induced RNA structural loss provides more accessible “landing pad” for YTHDF1, consequently promoting RNA degradation and reducing mRNA abundance (Fig. 7). It is also worth noting that in addition to YTHDF1, the binding of other factors could also be facilitated upon the increased structural accessibility to facilitate DHX36 regulation of post-transcriptional processes. For example, hnRNPC which requires less structured m^6A substrates [13] could also be recruited to function in modulating alternative splicing. It will thus be necessary to define structure-dependent DHX36 interactome in cells in the future. Altogether our findings support the emerging theme that RNA structure constitutes an important layer of gene regulatory determinants.

Materials and Methods

Cell culture

Human HEK293T cells (CRL-3216) and mouse C2C12 myoblast cells (CRL-1772) were obtained from American Type Culture Collection (ATCC) and cultured in DMEM medium (12800-017, Gibco) with 10% fetal bovine serum (FBS, 10270-106, Gibco) and 1% penicillin/streptomycin (P/S, 15140-122, Gibco) at 37°C in 5% CO2 incubator.

Generation of DHX36 knockout cells

For human HEK293T cells, DHX36 gene exons were input into http://crispor.tefor.net, and crRNAs were generated and selected. crRNAs were ligated to PX458 plasmid and synthesized by Genewiz (China). 0.1 million authenticated HEK293T cells were seeded on 24 well plates to culture in DMEM medium with 10% Heat inactivated fetal bovine serum, 100 units/ml of antibiotic antimycotic (Thermo Fisher Scientific, USA) at 37°C in 5% CO_2 incubator. After 24 hours, two 500ng ligated PX458 plasmid were transfected into cells using Lipofectamine® 2000 (Thermo Fisher Scientific, 11668019) according to the manufacturer's protocol. 48 hours later, cells were extracted and FACS-sorted (Sony SH800S cell sorter) according to GFP signal and positive cells were transferred to a new 96-well plate. Single clones were selected under microscope and expanded in a 6 well plate. After 4-7 days incubation, cells were collected to extract DNA for genotyping and protein for knockout detection. Mouse DHX36 knockout C2C12 myoblast cells were generated and used as previously described [22, 60].

In vivo chemical probing

For HEK293T cells, the WT and DHX36-KO cells were harvested in 1X PBS buffer (Thermo Fisher Scientific, 10010049) and probed with NAI (50mM in final) or 5% DMSO as negative control for 15min at 37°C, 500 rpm. Then DTT (200mM in final) was added immediately to quench each probing reaction. After spinning down the cells (~500g) for 3min at room temperature, total RNAs were extracted and quantified using RNeasy Plus Mini Kit (Qiagen, 74136) and Nanodrop ND-1000 Spectrophotometer. For C2C12 cells, the proliferating WT or Dhx36-KO myoblasts were harvested in 1X PBS buffer and probed with DMS (20mM in final) or 5% DMSO as negative control for 15 min at 37°C. Then DTT (200mM in final) was added immediately to quench each probing reaction. After spinning down the cells (~500g) for 3 min at room temperature, total RNAs were extracted using RNeasy Plus Mini Kit (Qiagen, 74136).

Gel-based identification of *in vivo* chemical probing for 5.8S rRNA

2μg *in vivo* NAI/DMS-probed total RNAs were dissolved in 5.5μl water, 1μl of 5μM Cy5-modified RT primer for 5.8S rRNA and 3μl of reverse transcription buffer with dNTPs (20mM Tris-HCl (pH 7.5), 4mM $MgCl_2$, 1mM DTT, 0.5mM dNTPs, 150mM LiCl in final) were denatured at 75°C for 3min. The reaction was cooled down to 37°C for 5min, and 0.5μl SuperScript III (Thermo Fisher Scientific, 18080093) was added and mixed quickly. The RT reaction was incubated at 50°C for 15min following 0.5μl of 2M NaOH addition at 95°C for 10min to degrade RNA template. 10μl 2X denaturing dye (95% formaldehyde, 20mM EDTA (pH 8.0), 20mM Tris-HCl (pH 7.5), orange G) was added and incubated at 95°C for 3min. The resultant reaction was kept on 60°C and loaded to 8% polyacrylamide-urea denaturing gel (containing 8.3M of urea) for electrophoresis. For the sequencing lanes, RNAs were dissolved in 4.5μl water; 1μl 10mM of ddATP/ddTTP/ddCTP/ddGTP

(Roche, 12352200) was added at the beginning.

Structure-seq library preparation

Detailed procedures for cDNA library preparation were described in two references [61] (for C2C12 libraries) and [62] (for HEK293T libraries) with slight modification. Briefly, each library was prepared with 500ng poly(A)-selected RNAs after 2 rounds of selection (Thermo Fisher Scientific, AM1922). The poly(A) RNAs were fragmented to around 300nt length at 95°C for 1min and purified using RNA clean and concentrator (Zymo research, R1016). The fragmented RNA was then subjected to a 5' dephosphorylation reaction at 37°C for 30min by adding rSAP (NEB, M0371L) and PNK enzyme (NEB, M0201S) in 1× T4 PNK buffer (NEB, B0201S). Next, the 3'adapter was ligated to the dephosphorylated RNA using T4 RNA ligase 2 KQ (NEB, M0373L) at 25°C for 1h. Excess adapters were digested and removed by adding RecJf (NEB, M0331) and 5' deadenylase (NEB, M0331) for 30min at 30°C followed by column purification (Zymo research, R1016). The following reverse transcription (RT) was performed in 1X RT buffer (20mM Tris, pH 7.5, 4mM MgCl2, 1mM DTT, 0.5mM dNTPs, 150mM LiCl) with SuperScript III enzyme (Thermo Scientific, 18080093) at 42°C for 40min. RNA was digested by 2M NaOH and the reaction was neutralized with 1M Tris-HCl (pH 7.5) followed by column purification (Zymo research, R1016). The 5'adapter (for C2C12 libraries) or dU adapter (for HEK293T libraries) was ligated to the cDNA with Quick T4 DNA ligase (NEB, M2200L) and incubated in 37°C overnight. For the C2C12 library, the ligated product was run on the 10% denaturing urea-TBE acrylamide gel (Thermo Scientific, EC68752BOX), and the 100–400nt region was cut and dissolved in 1X TEN250 buffer (1X TE 7.4, 0.25M NaCl) at 80°C for 30min followed by column purification (Zymo research, R1016). For the HEK293T libraries, the

ligated product was first purified by column (Zymo research, R1016), then USER II enzyme (NEB, M5509) was added to cleave the product followed by a second column purification (Zymo research, R1016). The purified product was used for PCR cycle test and amplification with different barcoded reverse primer. PCR products with 150-400 bp were then cut and purified with 2% agarose gel and column (Zymo research, D4008). Finally, all libraries were sequenced on the Illumina HiSeq System in 150bp paired end (PE) configuration.

RNA Bind-n-Seq (RBNS) assay

RHAU53 peptide with a His tag at C terminal was synthesized by Synpeptide Co Ltd and stored at -80°C. To perform the RBNS assay, we followed a modified version of the method described previously [63, 64] with modification. First, we generated a dsDNA template from a single-stranded 40 nt random DNA and reverse extension primer through an extension reaction using Superscript III reverse transcriptase (Thermo Fisher Scientific, 18080085). RNAs with a random region of 40nt were prepared by *in vitro* transcription (NEB, E2040S) using the dsDNA as template. We then heated the concentrated RNAs at 85°C for 5min in the presence of 150mM KCl or LiCl and allowed them to cool for at least 3 min to promote structural folding. Then the RNA library was incubated with an increasing concentration of RHAU53 (5, 20, 80, 320 and 1300nM) with binding reactions as previously described [64], with slight modifications. In this study, 10µl NEBExpress® Ni-NTA Magnetic Bead (NEB, S1423L) was used to replace the Dynabeads MyOne Streptavidin T1 in old method to pull-down the His tagged protein-RNA complexes. All wash and binding buffers contained either 150mM KCl or LiCl. Protein-RNA complexes were eluted in 1 X elution buffer (20 mM Tris-HCl (pH 7.5), 150mM KCl or LiCl, 500mM Imidazole (pH 7.4), 8M Urea). RNAs were

isolated as previously described [64] and reverse transcribed for PCR amplification and sequencing (See Structure-seq library preparation Method).

mRNA stability assay

WT or DHX36-KO HEK293T cells were treated with 5μg/ml actinomycin D (ThermoFisher Scientific, 11805017) for 0h, 4h and 8h separately. Cells were collected for total RNAs isolation using RNeasy Plus Mini Kit (Qiagen, 74136). The same amount of total RNAs from each sample were reversely transcribed with PrimeScript RT Master Mix (TaKaRa, RR036A). Diluted cDNAs were mixed with primers and SsoAdvanced Universal SYBR® Green Supermix (BioRad, 1725272) for qPCR amplification with CFX Connect Real-Time PCR System (BioRad). GAPDH gene was used for normalization.

RNA immunoprecipitation assay

WT or DHX36-KO 293T cells were washed with 1X PBS for two times and collected by centrifugation at 700g, 4°C for 5 min. Cell pellets were lysed with RIP lysis buffer (10mM HEPES, pH 7.0, 100mM KCl, 5mM $MgCl_2$, 0.5% NP-40, 1mM DTT, 100 units RNase-out and 1x protease inhibitor cocktail) on ice for 10 min. The supernatant was collected after centrifugation at 14,000 × g at 4°C for 15min. In total, 5 μg of antibodies against YTHDF1 (Proteintech 17479-1-AP) or isotype IgG (Santa Cruz Biotechnology, sc-2025) were incubated with 30μl of Protein G DynabeadsTM (ThermoFisher Scientific, 10003D) with rotation at RT for 1h followed by adding same volume of cell lysate to the lysate with further incubation with rotation at 4°C overnight. The beads were washed with ice cold RIP wash buffer (50mM Tris-HCl pH7.4, 150mM NaCl, 1mM

$MgCl_2$, 0.05% NP-40) for six times, of which Remove 1/3 volume were removed from the bead suspension during last wash for western blotting. Proteinase K was then added to the beads with incubation at 4°C for an hour. After discarding the supernatant from the final wash, Qiazol lysis reagent was added (Qiagen) to the sample for RNA extraction. Extracted RNAs were resuspended in 30µl of RNase-free water and cDNAs were obtained from reverse transcription for qPCR test (See above). 10% of cell lyates of each sample was collected followed by total RNA extraction and qPCR test for normalization.

Western blotting (WB)

Cells were harvest and lysed in RIPA reagent (Thermo Fisher Scientific, 89900) for 15 min. on ice. Total proteins were centrifuged (15000 rpm at 4°C) and determined using protein assay dye reagent (Bio-Rad, 500006). Subsequently, 25µg proteins were separated via 4-10% SDS-PAGE and transferred to PVDF membranes. Following blocking with 5% non-fat milk for 1 h at room temperature, the membrane was incubated overnight at 4°C with primary antibody dilution. After washing 3 times with 1X TBS-T buffer (150mM NaCl, 20mM Tris-HCl (pH 8.0) and 0.05% Tween 20) for 10min, the membrane was incubated with secondary antibody dilution for 1 h at room temperature. Subsequently, the membrane was washed 3 times with 1X TBS-T buffer for 10 min. After staining with Clarity Max Western ECL Substrate (Bio-Rad, 1705062), the signal was visualized using ChemiDoc™ Touch Imaging System. The primary antibodies used are as follows: DHX36 (Proteintech 13159-1-AP) and GAPDH (Santa Cruz, sc-32233). Secondary antibodies used are Goat anti Mouse IgG (H/L): HRP (Bio-Rad, STAR207P) and Goat anti Mouse IgG (H/L): HRP (Beyotime, A0208).

Structure-seq data analysis

Both Structure-seq data in HEK293T and C2C12 cells were processed using StructureFold2 [35]. The adapters were first removed using Cutadapt v1.15 [65] and the reads shorter than 20nt or with quality score lower than 30 were filtered out. The remaining reads were mapped to human or mouse transcriptome reference using Bowtie2 v2.3.3.1 [66] with default parameters. Human and mouse transcriptome references were respectively obtained from GENCODE v33 and vm24 database [67]. Next, the mapped reads with more than 3 mismatches or mismatch at the first base were removed using the sam_filter.py script. For each library, RT stops were counted using the sam_to_rtsc.py script. The correlation of RT stops between two replicates were determined using the rtsc_correlation.py script. The average RT coverage of each transcript in NAI or DMS-treated libraries was calculated using the rtsc_coverage.py script. For NAI-treated libraries, average coverage was calculated as the sum of RT stops within the transcript divided by the length of the transcript. For DMS-treated libraries, only adenines and cytosines were considered. Transcripts with average coverage higher than 1 in all replicates of all the treated WT and KO samples were saved, followed by the combination of RT stop counts across two biological replicates from each sample. The raw reactivity score for each nucleotide was calculated based on the modified formula as Yang et al. described [68]:

$$Reactivity_i = \frac{\ln\,(1+P_i)}{\sum_i \ln\,(1+P_i)\,/L} - \alpha\frac{\ln\,(1+M_i)}{\sum_i \ln(1+M_i)\,/L}$$

$$\alpha = \min(1, \sum_i \ln(1+P_i)\,/\sum_i \ln\,(1+M_i)\,)$$

where P_i and M_i respectively represent the RT stops of nucleotide i in NAI/DMS-treated and

DMSO-treated samples; L represents transcript length; α is a library size correction factor. The raw reactivity was then normalized by 2-8% method to generate final reactivity. Next, the splice_reacts_by_FASTA.py script was used to splice the reactivity profile of the entire transcript by the designated mRNA regions. The average reactivity and the Gini index of SHAPE reactivity of the entire transcript or the designated region was calculated using the react_statistics.py script. RNA structure folding constrained by reactivity score was performed using the ViennaRNA package [40]. The base-pairing probability of each nucleotide was extracted from the corresponding structure ensemble ".ps" file. The software dStruct [39] (parameter: reps_A = 2, reps_B = 2, min_length = 5, batches=T, check_signal_strength = T, check_nucs = T, check_quality = T) was used to identify the significant DRRs within DHX36 binding sites (FDR<0.25).

For 18S rRNA benchmarking, we respectively aligned the reads in HEK293T or C2C12 cells to human and mouse 18S rRNA reference (human: NR_145820.1; mouse: NR_003278.3). The RT stops and reactivity scores were calculated based on the same workflow as stated above. Finally, the reactivity scores were mapped to the phylogenetic structures of human or mouse 18S rRNA, which were obtained from CRW database [69], to evaluate the performance of our *in vivo* Structure-seq libraries.

Analysis of PAR-CLIP and CLIP-seq data for identification of DHX36 binding sites

Publicly available PAR-CLIP data (GSE105171) [37] were analyzed to identify the endogenous DHX36 binding sites. Since the use of 4-thiouridine (4SU) labelling on the transcripts restricts crosslinking to a single base and leads to T-to-C mutation during reverse transcription of crosslinked RNAs, the pipeline described in the CLIP Tool Kit (CTK) [38] was used to identify crosslinking sites

at single-nucleotide resolution. Briefly, 3'adapter sequences and low-quality reads were trimmed by Cutadapt v1.15 [65] (parameter: -n 1 -q 5 -m 20), followed by collapsing the exact duplicates with the same sequence. Then, we mapped the remaining reads to human hg38 genome reference using BWA v0.7.17 [70] (parameter: -n 0.06 -q 20). To achieve peak calling at single-nucleotide resolution, the crosslinking induced mutation sites (CIMS) mode of CTK was used. To improve the reliability, we defined the significant CIMS with FDR < 0.05 in both biological replicates as exact crosslink sites and the +/- 50nt of crosslink sites as DHX36 binding sites. DHX36 binding sites were annotated to the 5'UTR, CDS or 3'UTR regions based on the GENCODE human v33 annotation file [67].

CLIP-seq data (GSE151124) in C2C12 cells were analyzed using the same pipeline as previously described [22]. The adaptors and low-quality reads were trimmed using FastQC [71] and Trimmomatic [72]. Following duplicate removal, the remaining reads were aligned to mouse genome mm10 using Bowtie2 v2.3.3.1 [66] and peaks were called using Piranha v1.2.1 [73] (parameter: -p_threshold 0.05 -b 100). Annotation of the peaks to designated mRNA regions was based on GENCODE mouse vm24 annotation file [67].

RNA Bind-n-Seq data processing

RBNS data were processed using RBNS pipeline [64]. Briefly, 6mer motif frequency was calculated in each RHAU53-bound pool at 5 different concentrations (5nM, 20nM, 80nM, 320nM and 1300nM) and the input pool. Motif R value representing the enrichment level was defined as the frequency of each 6mer in the RHAU53-bound pool divided by the frequency in the input pool.

rG4 prediction and evaluation

rG4 prediction and classification were performed using our published strategy [22]. The script can be accessed in Github repository (https://github.com/jieyuanCUHK/DHX36_paper). rG4 score for each rG4 was evaluated by the R package pqsfinder [74] (parameter: strand = "+", run_max_len = 3L, loop_min_len = 1L, loop_max_len = 21L, min_score = 1L). In this scoring system, rG4s with 3 G-quartets, shorter loops, and less bulges were assigned with higher scores because of their high stability [75].

RNA-seq data analysis

RNA-seq data from the chromatin fraction or whole-cell in WT and DHX36-KO HEK293 cells were used in our study (GSE105175) [37]. All these data were analyzed using the same pipeline. First, the 3'adapters and low quality bases were trimmed by Cutadapt [65]. Next, the remaining reads were mapped to human hg38 genome reference using HISAT2 v2.0.4 [76] with default parameters. The uniquely mapped reads were then counted using featureCounts v2.0.1 [77]. To obtain the DHX36 loss-induced differential expression profile, we used the R package DESeq2 [78] to normalize the read counts of each gene and evaluate the statistical significance and the fold change of the RNA abundance upon DHX36 loss in both whole-cell and chromatin fraction. The post-transcriptional fold change (pFC) was defined as the fold change in chromatin fraction divided by the fold change in whole cell. The genes with pFC greater than 1.5 or lower than 1/1.5 were defined as post-transcriptionally up- or down-regulated genes.

Analysis of miCLIP data for identification of m^6A modification and YTHDF1 binding sites

Publicly available miCLIP data in WT HEK293 (GSE63753) [47] and HEK293T cells (GSE122948)

[79] were used to identify m^6A modification at single-nucleotide resolution. For miCLIP in HEK293 cells, both Synaptic Systems (SySy) and Abcam libraries were collected and analyzed as demonstrated [47]. First, the raw reads were trimmed using Cutadapt v1.15 [65] and demultiplexed based on the experimental barcodes using pyCRAC tool [80]. Next, the replicates were combined followed by PCR duplicate removal. For the paired-end data of Abcam libraries, reverse reads were reverse complemented and assigned with random barcodes. The processed reads were mapped to human hg38 genome reference using BWA v0.7.17 [70]. The CIMS pipeline in CTK [38] was used to identify the C to T mutations. For single-end data of SySy libraries, following read mapping, the CITS pipeline in CTK [38] was used to call truncation sites. The significant C to T mutation and truncation sites were selected as the exact crosslink sites. The crosslink sites identified in either Abcam or SySy libraries were defined as the m^6A modified sites. For miCLIP data in HEK293T cells, the same analytical workflow for Abcam libraries was used to identify significant crosslink sites. The crosslink sites identified by at least one miCLIP data were defined as m^6A sites.

Analysis of iCLIP data for identification of YTHDF1 binding sites

Identification of YTHDF1 binding sites was based on iCLIP data in HEK293T cells (GSE78030). First, Cutadapt v1.15 was used to trim the raw reads and filter out the low-quality reads. Next, the exact duplicates with same sequences were removed and the remaining reads were mapped to human hg38 genome reference using BWA v0.7.17 [70]. The uniquely mapped reads were saved and potential PCR duplicates were removed to obtain unique CLIP tags. The unique tags for each replicate were merged and the CITS pipeline in CTK was used to identify crosslink-induced truncation sites. The significant truncation sites were defined as YTHDF1 binding sites ($P<0.05$).

Motif analysis of m^6A-modified sites and YTHDF1 binding sites

Single-nucleotide m^6A-modified sites and YTHDF1 binding sites were extended for 5nt for both sides. Next, HOMER [81] was used to discover the m^6A and YTHDF1 motifs *de novo* within the extended sites (parameter: -size 10 -len 5 -norevopp -rna) and determine the enrichment of m6A and YTHDF1 motifs within 3'UTR binding of DHX36 (parameter: -len 5,6,7,8,9,10 -mknown <m^6A/YTHDF1 motif> -norevopp -rna).

Analysis of 4SU-TT-seq data for identification of YTHDF1 degradation targets

The half-lives of mRNAs in WT and YTHDF1-KO HEK293 cells were obtained from the published 4SU-TT-seq data (GSE143994) [25]. The fold changes of half-lives (YTHDF1-KO/WT) in 3 biological replicates were respectively calculated and then averaged to overall fold changes. Finally, we defined the mRNAs with overall fold changes greater than 1 as YTHDF1-induced degradation mRNAs.

Oligonucleotides

The oligonucleotides used in this study can be accessed in Supplementary Table S8.

Data availability

Structure-seq and RBNS data used in this study have been deposited in Gene Expression Omnibus (GEO) database under the accession codes GSE237160 (Structure-seq), GSE237161 (RBNS).

Acknowledgement

This work was supported by National Key R&D Program of China to H.W. (2022YFA0806003); General Research Funds (GRF) from the Research Grants Council (RGC) of the Hong Kong Special Administrative Region (14115319, 14100620, 14106521 and 14105823 to H.W.; 14120420, 14103522 and 14105123 to H.S.; CityU 11100222, CityU 11100421, CityU 11101519 to C.K.K.); the National Natural Science Foundation of China (NSFC) (grant no. 82172436 to H.W.); the research funds from Health@InnoHK program launched by Innovation Technology Commission, the Government of the Hong Kong SAR, China to H.W.; Collaborative Research Fund (CRF) from RGC to H.W. (C6018-19GF); Theme-based Research Scheme (TRS) from RGC (project number: T13-602/21-N); Hong Kong Epigenomics Project (EpiHK) Fund to H.W. and H.S.; Area of Excellence Scheme (AoE) from RGC (project number: AoE/M-402/20); Health and Medical Research Fund (HMRF) from Health Bureau of the Hong Kong Special Administrative Region, China (project Code: 10210906 and 08190626 to H.W.); CUHK Direct Grant to X.C. (project No.: 2022.038); Shenzhen Basic Research Project (JCYJ20180507181642811) to C.K.K., National Natural Science Foundation of China (NSFC) Excellent Young Scientists Fund (Hong Kong and Macau) Project (32222089) to C.K.K.; Croucher Foundation Project (9509003) to C.K.K.; State Key Laboratory of Marine Pollution Director Discretionary Fund (DDF/0008) to C.K.K.; Seed Collaborative Research Fund (SCRF/0037, SCRF/0040) to C.K.K.; City University of Hong Kong projects (9678302 and 9667222) to C.K.K..

Author contributions

Y.Z., X.C. and H.W. conceived the research. Y.Z. designed and performed all computational analyses. K.L. constructed the DHX36 KO cell line. J.Z. constructed Structure-seq library, RBNS library and performed experimental validation assisted by X.C. H.S. supervised computational analyses. Y.D. and C.K.K. supervised RNA Structure-seq and RBNS experiments and analyses. C.K.K. and H.W. supervised experimental validation. Y.Z., J.Z., X.C., C.K.K. and H.W. wrote the manuscript with input from all authors.

Conflict of interest

The authors declare no competing interests.

Figure legends

Figure 1. *In vivo* RNA structurome profiling unveils DHX36 depletion-induced global loss of RNA structures. (A) Left: schematic illustration of the CRISPR-Cas9 mediated generation of DHX36 knockout (KO) in HEK293T cells. 169 bp of exon 1 of DHX36 gene was deleted by two single-guide RNAs and CRISPR-Cas9. Right: western blot confirmed the inactivation of DHX36 in KO cells with GAPDH as the loading control. (B) Schematic illustration of *in vivo* structure mapping in WT and DHX36-KO cells. Orange circle, SHAPE modification; NGS, next-generation sequencing; RT, reverse transcription. (C) Sequencing gel for 5.8S rRNA showing the RT stops induced by NAI modification. (D) The average SHAPE reactivity score and (E) Gini index of reactivity scores of all mRNAs in WT and DHX36-KO. Mann-Whitney test was used to calculate the statistical significance. The fold change (FC) between the KO vs WT is shown. (F) Top: the binned average reactivity across the length of 5'UTRs (25 bins), CDSs (50 bins) and 3'UTRs (25 bins) of all mRNAs. Bottom: The binned ΔReactivity (KO-WT) across the above regions. Shaded area represents 95% confidence intervals of the average ΔReactivity of each bin calculated by paired two-sided Student's t-test.

Figure 2. DHX36 binding induces mRNA structural loss and gained accessibility. (A) Schematic illustration of the workflow for analyzing PAR-CLIP and Structure-seq data to identify DHX36 binding-induced structure remodeling. (B) DHX36 binding sites were identified by analyzing PAR-CLIP data and the distribution in 5'UTRs, CDSs and 3'UTRs is shown. (C) Metagene profile showing the distribution of DHX36 binding sites across the human transcriptome. (D) rG4 formation was predicted in DHX36 binding sites and the distribution of each subtype is shown. (E) The average

SHAPE reactivity score and Gini index of the reactivity scores of DHX36-bound mRNAs. Mann-Whitney test was used to calculate the statistical significance. The fold change (FC) between the KO vs WT is shown. (F) Comparison of ΔReactivity and ΔGini (KO-WT) between DHX36-bound and unbound mRNAs. (G) The binned average reactivity (top) and ΔReactivity (bottom) across the length of 5'UTRs (25 bins), CDSs (50 bins) and 3'UTRs (25 bins) of DHX36-bound mRNAs. Shaded area represents 95% confidence intervals of the average ΔReactivity of each bin calculated by paired two-sided Student's t-test. (H) The average reactivity of 5'UTR, CDS, and 3'UTR of DHX36-bound mRNAs. Mann-Whitney test was used to calculate the statistical significance. (I) Scatterplot showing regional ΔReactivity vs. GC content of the designated regions. r and P represent the correlation coefficient and statistical significance calculated by Pearson correlation test. (J) The proportion of DHX36 depletion-induced DRRs located within (+DHX36) and outside (-DHX36) DHX36 binding sites. (K) Metagene profiles showing the distribution of DHX36-induced DRRs across different regions of DHX36-bound mRNAs. (L) The distribution of DRRs across the mRNAs with DHX36 binding to 5'UTR (top), CDS (middle) or 3'UTR (bottom) only. In each panel, line plot shows the location of DHX36 binding sites and heatmap shows the DRR enrichment. The colors of the heatmap encode the amount of DRRs. (M) ΔReactivity (KO-WT) of each nucleotide of *PYCR1* and *CCNA2* mRNA. DRRs and DHX36 binding sites are highlighted in the shaded areas and green arrow respectively. ΔR and P represent the average difference in reactivity of the designated mRNA region and the significance calculated by Mann-Whitney test.

Figure 3. DHX36 induces localized structural loss of 3'UTR binding sites. (A) Average SHAPE

reactivity (top), BPP (middle), and nucleotide composition (bottom) across DHX36 binding sites. Position 0 represents the exact crosslink site identified by PAR-CLIP data. (B) The percentage of DHX36 binding sites with or without DRRs. (C) rG4 formation was predicted in DRR-containing DHX36 binding sites and the distribution of each subtype is shown. (D) Comparison of average SHAPE reactivity across DHX36 binding sites with and without rG4s in WT and DHX36-KO. (E) Comparison of average SHAPE reactivity across DHX36 binding sites located in 5'UTR (top), CDS (middle) and 3'UTR (bottom) in WT and DHX36-KO. (F) The percentage of DHX36-bound DRRs in 5'UTR, CDS and 3'UTR. (G) Barplot showing the SHAPE reactivity of the DHX36 binding site within mRNA *JUN* in WT and DHX36-KO. (H) Illustration of the folded structure of the DHX36 binding site within mRNA *JUN* in WT and DHX36-KO. Nucleotides were color-coded based on the SHAPE reactivity scores. (I) Heatmap depicting the coefficients of the explanatory variables in the linear regression models, including localized GC content of DHX36 binding sites, regional GC content and ln(length) of DHX36-bound mRNA regions. Rows represent the models designed for 4 kinds of response variables: the localized ΔReactivity (KO-WT) of all, 5'UTR, CDS and 3'UTR binding sites.

Figure 4. DHX36 binding induced 3'UTR structural change is associated with post-transcriptional regulation of mRNA abundance. (A) Schematic illustration showing the method for defining DHX36-induced post-transcriptional regulatory effect. The post-transcriptional fold change (pFC) of mRNA abundance was calculated by dividing the fold change in chromatin fraction by that in whole cell. (B) Scatterplot showing the definition of pUGs and pDGs based on the

pFC of mRNA abundance. (C) Venn diagram showing the overlapping between DHX36-bound mRNAs and pUGs or pDGs. Statistical significance was calculated by Chi-square test. (D) Comparison of pFCs of DHX36-bound mRNAs and all protein-coding genes. (E) Comparison of ΔReactivity of pDG and pUG targets. (F-I) Scatterplots showing the correlations of mRNA abundance pFCs with reactivity changes of (F) entire mRNAs, (G) 5'UTRs, (H) CDSs and (I) 3'UTRs of DHX36-bound mRNAs. r and P represent the correlation coefficient and statistical significance calculated by Pearson correlation test. (J) Average SHAPE reactivity across DHX36 binding sites within the designated regions of pUGs and pDGs. The colored horizontal lines represent the means of average reactivity across the binding sites. Position 0 represents the exact crosslinking sites identified by PAR-CLIP data. (K) ΔReactivity of DHX36 binding sites within the designated regions of pUGs and pDGs. Error bars represent 95% confidence intervals (CI) of the mean of ΔReactivity. P values were calculated by unpaired two-sided Student's t-test.

Figure 5. DHX36-induced RNA structural accessibility facilitates m^6A dependent YTDHF1 binding and RNA degradation. (A) Schematic illustration showing the investigation of DHX36/m^6A/YTHDF1 co-regulation of mRNA abundance via RNA structure remodeling. (B) Significant enrichment of m^6A and YTHDF1 motifs in the 3'UTR binding sites of DHX36. (C-D) Enrichment of m^6A and YTHDF1 binding within DHX36 binding sites compared to random sites. The randomly selected sites are in equal numbers, equal length, and from the same 3'UTR with the DHX36 binding sites. Statistical significance was calculated by Monte Carlo method. (E) Comparison of pFCs between DHX36-bound mRNAs with m^6A or m^6A/YTHDF1 within 3'UTRs

and those without m^6A/YTHDF1. Statistical significance was calculated by unpaired two-sided Student's t-test. (E) Identification of DHX36/m^6A/YTHDF1 degradation targets by comparing DHX36 pUG targets with YTHDF1 degradation targets. (F) Venn diagram showing significant overlapping between 3'UTR YTHDF1 binding sites and DRR-containing DHX36 binding sites within 3'UTRs. Statistical significance in (E) and (F) was calculated by hypergeometric test. (H) Comparison of average reactivity and BPP of the regions surrounding m^6A sites within DHX36-bound mRNAs in WT and DHX36-KO cells. Position 0 and green area denote m^6A residues and m^6A motif respectively.

Figure 6. DHX36 facilitates YTHDF1 binding to decrease mRNA stability on selected targets. (A) Genome tracks showing RNA abundance in chromatin fraction and whole cell, DHX36 binding sites, m^6A sites, YTHDF1 binding sites, and SHAPE reactivity of the DHX36 binding sites in mRNAs EZR, MEPCE, PHF23 and ZNF768. (B) Illustration of the folded structures of the DHX36 binding sites within the above mRNAs in WT and DHX36-KO cells. m^6A and YTHDF1 binding sites are highlighted using yellow lines. Nucleotides are color-coded based on the SHAPE reactivity scores. (C) Abundance of the above mRNAs in WT and DHX36-KO cells were quantified by RT-qPCR. (D) mRNA stability of the above mRNAs was determined by quantifying the mRNA abundance 0h, 4h and 8h after actinomycin D treatment. qRT-PCR was used for mRNA quantification. The mRNA abundance detected at each time point is represented as the fraction of total mRNA amount quantified at time 0h and normalized on the GAPDH abundance. (E) mRNA half-life of the above mRNAs in WT and YTHDF1-KO was determined by analyzing 4SU-TT-seq

data. (F) RIP assay was performed in WT and DHX36-KO cells with an YTHDF1 antibody and enrichment of the immunoprecipitated YTHDF1 and GAPDH proteins were assessed by western blotting. IgG was used as negative control. (G) The enrichment of the representative mRNAs in the above RIP was detected by qPCR. Individual mRNA expression from total RNA from 10% cell lysate input was used for normalization. The relative enrichment was normalized by input (n=3). Statistical significance was calculated by Student's t-test. $^{***}P<0.001$, $^{**}P<0.01$, $^{*}P<0.05$. (H) Western blot confirmed the unaltered protein levels of YTHDF1 in WT and DHX36-KO cells.

Figure 7. Schematic illustration of the functional mechanism of DHX36-induced structure change in regulating the activity of YTHDF1 binding and target mRNA degradation. DHX36 binds to and resolves the structured sites. The increased structural accessibility of DHX36-bound m^6A sites promotes m^6A dependent YTHDF1 binding to promote target mRNA degradation.

Reference

1. Wang, X.W., et al., *RNA structure probing uncovers RNA structure-dependent biological functions.* Nat Chem Biol, 2021. **17**(7): p. 755-766.
2. Ding, Y., et al., *In vivo genome-wide profiling of RNA secondary structure reveals novel regulatory features.* Nature, 2014. **505**(7485): p. 696-700.
3. Spitale, R.C., et al., *Structural imprints in vivo decode RNA regulatory mechanisms*. Nature, 2015. **519**(7544): p. 486-90.
4. Weng, X., et al., *Keth-seq for transcriptome-wide RNA structure mapping.* Nat Chem Biol, 2020. **16**(5): p. 489-492.
5. Incarnato, D., et al., *Genome-wide profiling of mouse RNA secondary structures reveals key features of the mammalian transcriptome.* Genome Biol, 2014. **15**(10): p. 491.
6. Corley, M., M.C. Burns, and G.W. Yeo, *How RNA-Binding Proteins Interact with RNA: Molecules and Mechanisms*. Mol Cell, 2020. **78**(1): p. 9-29.
7. Georgakopoulos-Soares, I., G.E. Parada, and M. Hemberg, *Secondary structures in RNA synthesis, splicing and translation.* Comput Struct Biotechnol J, 2022. **20**: p. 2871-2884.
8. Spitale, R.C. and D. Incarnato, *Probing the dynamic RNA structurome and its functions*. Nat Rev Genet, 2023. **24**(3): p. 178-196.
9. Wang, J., et al., *Genome-wide RNA structure changes during human neurogenesis modulate gene regulatory networks.* Mol Cell, 2021. **81**(23): p. 4942-4953 e8.
10. Jin, Y., Y. Yang, and P. Zhang, *New insights into RNA secondary structure in the alternative splicing of pre-mRNAs.* RNA Biol, 2011. **8**(3): p. 450-7.
11. Shepard, P.J. and K.J. Hertel, *Conserved RNA secondary structures promote alternative splicing*. RNA, 2008. **14**(8): p. 1463-9.
12. Fischer, J.W., et al., *Structure-Mediated RNA Decay by UPF1 and G3BP1*. Mol Cell, 2020. **78**(1): p. 70-84 e6.
13. Liu, N., et al., *N(6)-methyladenosine-dependent RNA structural switches regulate RNA-protein interactions*. Nature, 2015. **518**(7540): p. 560-4.
14. Sloan, K.E. and M.T. Bohnsack, *Unravelling the Mechanisms of RNA Helicase Regulation.* Trends Biochem Sci, 2018. **43**(4): p. 237-250.
15. Srinivasan, S., et al., *Function of Auxiliary Domains of the DEAH/RHA Helicase DHX36 in RNA Remodeling.* J Mol Biol, 2020. **432**(7): p. 2217-2231.
16. Chen, M.C., et al., *Structural basis of G-quadruplex unfolding by the DEAH/RHA helicase DHX36.* Nature, 2018. **558**(7710): p. 465-469.
17. Kharel, P., et al., *Properties and biological impact of RNA G-quadruplexes: from order to turmoil and back.* Nucleic Acids Res, 2020. **48**(22): p. 12534-12555.
18. Herviou, P., et al., *hnRNP H/F drive RNA G-quadruplex-mediated translation linked to genomic instability and therapy resistance in glioblastoma.* Nat Commun, 2020. **11**(1): p. 2661.
19. Simko, E.A.J., et al., *G-quadruplexes offer a conserved structural motif for NONO recruitment to NEAT1 architectural lncRNA.* Nucleic Acids Res, 2020. **48**(13): p. 7421-7438.
20. Schult, P. and K. Paeschke, *The DEAH helicase DHX36 and its role in*

G-quadruplex-dependent processes. Biol Chem, 2021. **402**(5): p. 581-591.
21. Murat, P., et al., *RNA G-quadruplexes at upstream open reading frames cause DHX36- and DHX9-dependent translation of human mRNAs.* Genome Biol, 2018. **19**(1): p. 229.
22. Chen, X., et al., *Translational control by DHX36 binding to 5'UTR G-quadruplex is essential for muscle stem-cell regenerative functions.* Nat Commun, 2021. **12**(1): p. 5043.
23. Newman, M., et al., *The G-Quadruplex-Specific RNA Helicase DHX36 Regulates p53 Pre-mRNA 3'-End Processing Following UV-Induced DNA Damage.* J Mol Biol, 2017. **429**(21): p. 3121-3131.
24. Yang, Y., et al., *Dynamic transcriptomic m(6)A decoration: writers, erasers, readers and functions in RNA metabolism.* Cell Res, 2018. **28**(6): p. 616-624.
25. Li, J., et al., *YTHDF1 promotes mRNA degradation via YTHDF1-AGO2 interaction and phase separation.* Cell Prolif, 2021: p. e13157.
26. Zaccara, S. and S.R. Jaffrey, *A Unified Model for the Function of YTHDF Proteins in Regulating m(6)A-Modified mRNA.* Cell, 2020. **181**(7): p. 1582-1595 e18.
27. Wang, S., et al., *N6-Methyladenosine Reader YTHDF1 Promotes ARHGEF2 Translation and RhoA Signaling in Colorectal Cancer.* Gastroenterology, 2022. **162**(4): p. 1183-1196.
28. Wang, X., et al., *N(6)-methyladenosine Modulates Messenger RNA Translation Efficiency.* Cell, 2015. **161**(6): p. 1388-99.
29. Liu, N., et al., *N6-methyladenosine alters RNA structure to regulate binding of a low-complexity protein.* Nucleic Acids Res, 2017. **45**(10): p. 6051-6063.
30. Meiser, N., N. Mench, and M. Hengesbach, *RNA secondary structure dependence in METTL3-METTL14 mRNA methylation is modulated by the N-terminal domain of METTL3.* Biol Chem, 2020. **402**(1): p. 89-98.
31. Han, Z., et al., *Crystal structure of the FTO protein reveals basis for its substrate specificity.* Nature, 2010. **464**(7292): p. 1205-9.
32. Feng, C., et al., *Crystal structures of the human RNA demethylase Alkbh5 reveal basis for substrate recognition.* J Biol Chem, 2014. **289**(17): p. 11571-11583.
33. Zhang, Z., et al., *The YTH domain is a novel RNA binding domain.* J Biol Chem, 2010. **285**(19): p. 14701-10.
34. Ding, Y., et al., *Genome-wide profiling of in vivo RNA structure at single-nucleotide resolution using structure-seq.* Nat Protoc, 2015. **10**(7): p. 1050-66.
35. Tack, D.C., et al., *StructureFold2: Bringing chemical probing data into the computational fold of RNA structural analysis.* Methods, 2018. **143**: p. 12-15.
36. Sun, L., et al., *RNA structure maps across mammalian cellular compartments.* Nat Struct Mol Biol, 2019. **26**(4): p. 322-330.
37. Sauer, M., et al., *DHX36 prevents the accumulation of translationally inactive mRNAs with G4-structures in untranslated regions.* Nat Commun, 2019. **10**(1): p. 2421.
38. Shah, A., et al., *CLIP Tool Kit (CTK): a flexible and robust pipeline to analyze CLIP sequencing data.* Bioinformatics, 2017. **33**(4): p. 566-567.
39. Choudhary, K., et al., *dStruct: identifying differentially reactive regions from RNA structurome profiling data.* Genome Biol, 2019. **20**(1): p. 40.
40. Lorenz, R., et al., *ViennaRNA Package 2.0.* Algorithms Mol Biol, 2011. **6**: p. 26.

41. Peeri, M. and T. Tuller, *High-resolution modeling of the selection on local mRNA folding strength in coding sequences across the tree of life*. Genome Biol, 2020. **21**(1): p. 63.
42. Krishnan, N.M., H. Seligmann, and B.J. Rao, *Relationship between mRNA secondary structure and sequence variability in Chloroplast genes: possible life history implications*. BMC Genomics, 2008. **9**: p. 48.
43. Waldron, J.A., et al., *mRNA structural elements immediately upstream of the start codon dictate dependence upon eIF4A helicase activity.* Genome Biol, 2019. **20**(1): p. 300.
44. Holmqvist, E., et al., *Global Maps of ProQ Binding In Vivo Reveal Target Recognition via RNA Structure and Stability Control at mRNA 3' Ends*. Mol Cell, 2018. **70**(5): p. 971-982 e6.
45. Rasekhian, M., et al., *The Role of 3'UTR of RNA Viruses on mRNA Stability and Translation Enhancement.* Mini Rev Med Chem, 2021. **21**(16): p. 2389-2398.
46. Schwerk, J. and R. Savan, *Translating the Untranslated Region.* J Immunol, 2015. **195**(7): p. 2963-71.
47. Linder, B., et al., *Single-nucleotide-resolution mapping of m6A and m6Am throughout the transcriptome.* Nat Methods, 2015. **12**(8): p. 767-72.
48. Patil, D.P., et al., *m(6)A RNA methylation promotes XIST-mediated transcriptional repression.* Nature, 2016. **537**(7620): p. 369-373.
49. Fleming, A.M., N.L.B. Nguyen, and C.J. Burrows, *Colocalization of m(6)A and G-Quadruplex-Forming Sequences in Viral RNA (HIV, Zika, Hepatitis B, and SV40) Suggests Topological Control of Adenosine N (6)-Methylation.* ACS Cent Sci, 2019. **5**(2): p. 218-228.
50. Jara-Espejo, M., A.M. Fleming, and C.J. Burrows, *Potential G-Quadruplex Forming Sequences and N(6)-Methyladenosine Colocalize at Human Pre-mRNA Intron Splice Sites.* ACS Chem Biol, 2020. **15**(6): p. 1292-1300.
51. Xu, C., et al., *Structural Basis for the Discriminative Recognition of N6-Methyladenosine RNA by the Human YT521-B Homology Domain Family of Proteins.* J Biol Chem, 2015. **290**(41): p. 24902-13.
52. Li, J., et al., *YTHDF1 promotes mRNA degradation via YTHDF1-AGO2 interaction and phase separation.* Cell Prolif, 2022. **55**(1): p. e13157.
53. Varshney, D., et al., *RNA G-quadruplex structures control ribosomal protein production.* Sci Rep, 2021. **11**(1): p. 22735.
54. Nie, J., et al., *Post-transcriptional Regulation of Nkx2-5 by RHAU in Heart Development.* Cell Rep, 2015. **13**(4): p. 723-732.
55. Huang, W., et al., *Yin Yang 1 contains G-quadruplex structures in its promoter and 5'-UTR and its expression is modulated by G4 resolvase 1*. Nucleic Acids Res, 2012. **40**(3): p. 1033-49.
56. Maltby, C.J., et al., *A 5' UTR GGN repeat controls localisation and translation of a potassium leak channel mRNA through G-quadruplex formation.* Nucleic Acids Res, 2020. **48**(17): p. 9822-9839.
57. Wang, J., et al., *Genome-wide RNA structure changes during human neurogenesis modulate gene regulatory networks.* Mol Cell, 2021.
58. Lai, Y.H., et al., *Genome-Wide Discovery of DEAD-Box RNA Helicase Targets Reveals RNA Structural Remodeling in Transcription Termination.* Genetics, 2019. **212**(1): p. 153-174.

59. Youn, J.Y., et al., *High-Density Proximity Mapping Reveals the Subcellular Organization of mRNA-Associated Granules and Bodies.* Mol Cell, 2018. **69**(3): p. 517-532 e11.
60. Chen, X., et al., *Lockd promotes myoblast proliferation and muscle regeneration via binding with DHX36 to facilitate 5' UTR rG4 unwinding and Anp32e translation.* Cell Rep, 2022. **39**(10): p. 110927.
61. Yeung, P.Y., et al., *Systematic evaluation and optimization of the experimental steps in RNA G-quadruplex structure sequencing.* Sci Rep, 2019. **9**(1): p. 8091.
62. Zhao, J., et al., *Enhanced transcriptome-wide RNA G-quadruplex sequencing for low RNA input samples with rG4-seq 2.0.* BMC Biology, 2022. **20**(1).
63. Goering, R., et al., *FMRP promotes RNA localization to neuronal projections through interactions between its RGG domain and G-quadruplex RNA sequences.* Elife, 2020. **9**.
64. Dominguez, D., et al., *Sequence, Structure, and Context Preferences of Human RNA Binding Proteins*. Mol Cell, 2018. **70**(5): p. 854-867 e9.
65. Martin, M., *Cutadapt removes adapter sequences from high-throughput sequencing reads*. 2011, 2011. **17**(1): p. 3 %J EMBnet.journal.
66. Langmead, B. and S.L. Salzberg, *Fast gapped-read alignment with Bowtie 2.* Nat Methods, 2012. **9**(4): p. 357-9.
67. Frankish, A., et al., *GENCODE reference annotation for the human and mouse genomes*. Nucleic Acids Res, 2019. **47**(D1): p. D766-D773.
68. Yang, M., et al., *Intact RNA structurome reveals mRNA structure-mediated regulation of miRNA cleavage in vivo.* Nucleic Acids Res, 2020. **48**(15): p. 8767-8781.
69. Cannone, J.J., et al., *The comparative RNA web (CRW) site: an online database of comparative sequence and structure information for ribosomal, intron, and other RNAs.* BMC Bioinformatics, 2002. **3**: p. 2.
70. Li, H. and R. Durbin, *Fast and accurate long-read alignment with Burrows-Wheeler transform.* Bioinformatics, 2010. **26**(5): p. 589-95.
71. Wingett, S.W. and S. Andrews, *FastQ Screen: A tool for multi-genome mapping and quality control*. F1000Res, 2018. **7**: p. 1338.
72. Bolger, A.M., M. Lohse, and B. Usadel, *Trimmomatic: a flexible trimmer for Illumina sequence data.* Bioinformatics, 2014. **30**(15): p. 2114-20.
73. Uren, P.J., et al., *Site identification in high-throughput RNA-protein interaction data.* Bioinformatics, 2012. **28**(23): p. 3013-20.
74. Hon, J., et al., *pqsfinder: an exhaustive and imperfection-tolerant search tool for potential quadruplex-forming sequences in R.* Bioinformatics, 2017. **33**(21): p. 3373-3379.
75. Jana, J., et al., *Structural motifs and intramolecular interactions in non-canonical G-quadruplexes.* RSC Chem Biol, 2021. **2**(2): p. 338-353.
76. Kim, D., et al., *Graph-based genome alignment and genotyping with HISAT2 and HISAT-genotype.* Nat Biotechnol, 2019. **37**(8): p. 907-915.
77. Liao, Y., G.K. Smyth, and W. Shi, *featureCounts: an efficient general purpose program for assigning sequence reads to genomic features.* Bioinformatics, 2014. **30**(7): p. 923-30.
78. Love, M.I., W. Huber, and S. Anders, *Moderated estimation of fold change and dispersion for RNA-seq data with DESeq2.* Genome Biol, 2014. **15**(12): p. 550.

79. Boulias, K., et al., *Identification of the m(6)Am Methyltransferase PCIF1 Reveals the Location and Functions of m(6)Am in the Transcriptome.* Mol Cell, 2019. **75**(3): p. 631-643.e8.
80. Webb, S., et al., *PAR-CLIP data indicate that Nrd1-Nab3-dependent transcription termination regulates expression of hundreds of protein coding genes in yeast.* Genome Biol, 2014. **15**(1): p. R8.
81. Heinz, S., et al., *Simple combinations of lineage-determining transcription factors prime cis-regulatory elements required for macrophage and B cell identities.* Mol Cell, 2010. **38**(4): p. 576-89.

Zhang Y and Zhao J et. al. Figure 1

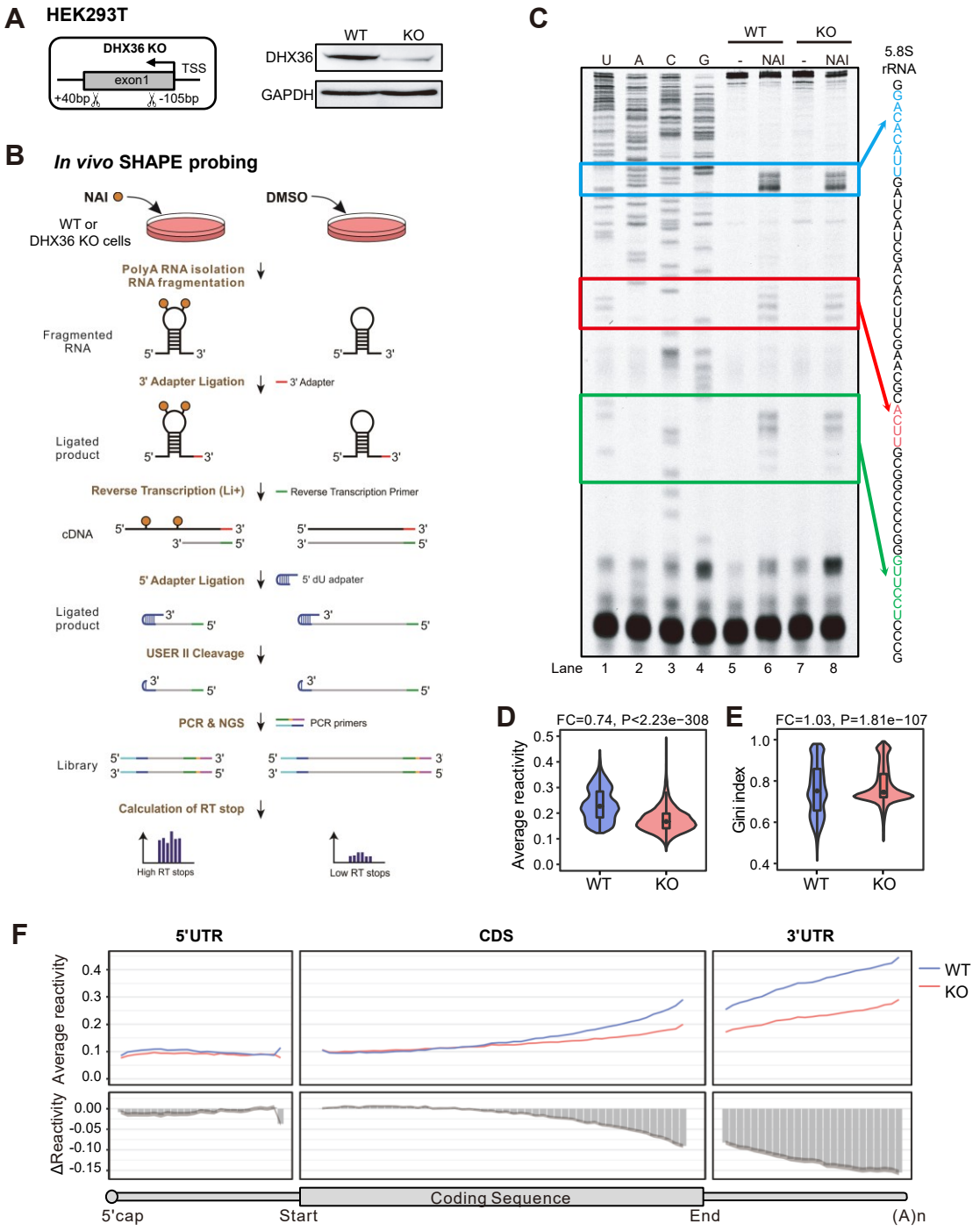

Zhang Y and Zhao J et. al. Figure 2

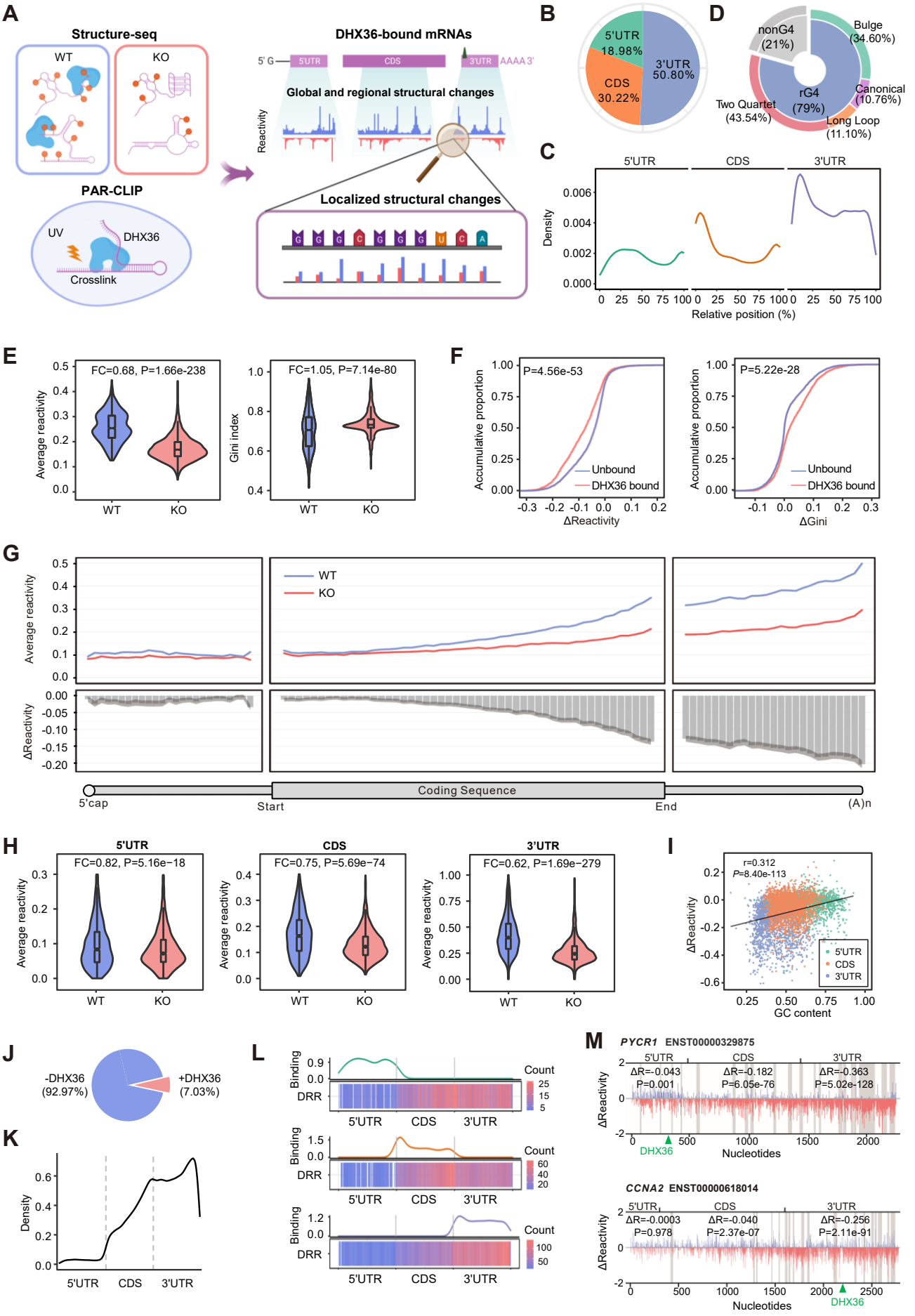

Zhang Y and Zhao J et. al. Figure 3

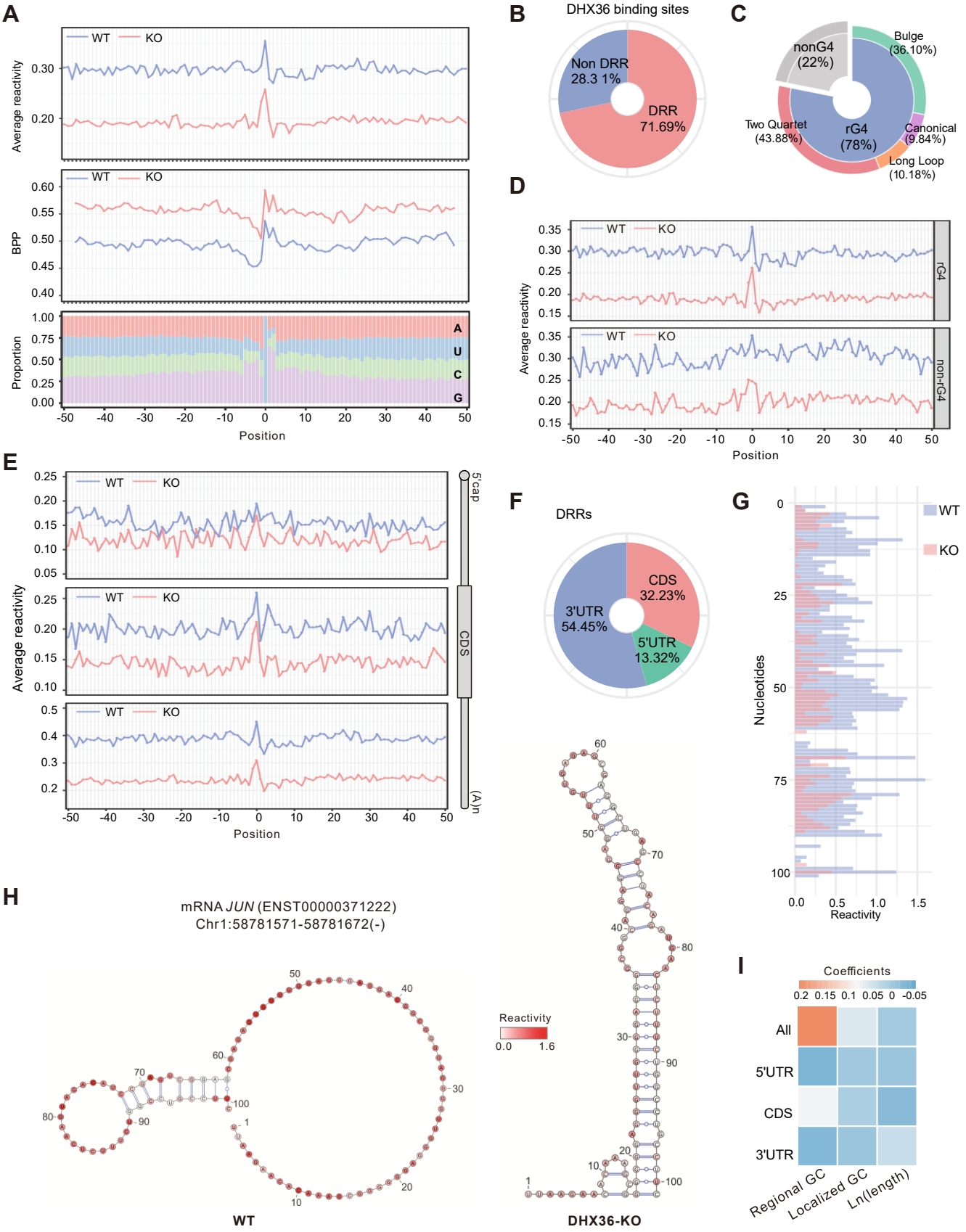

Zhang Y and Zhao J et. al. Figure 4

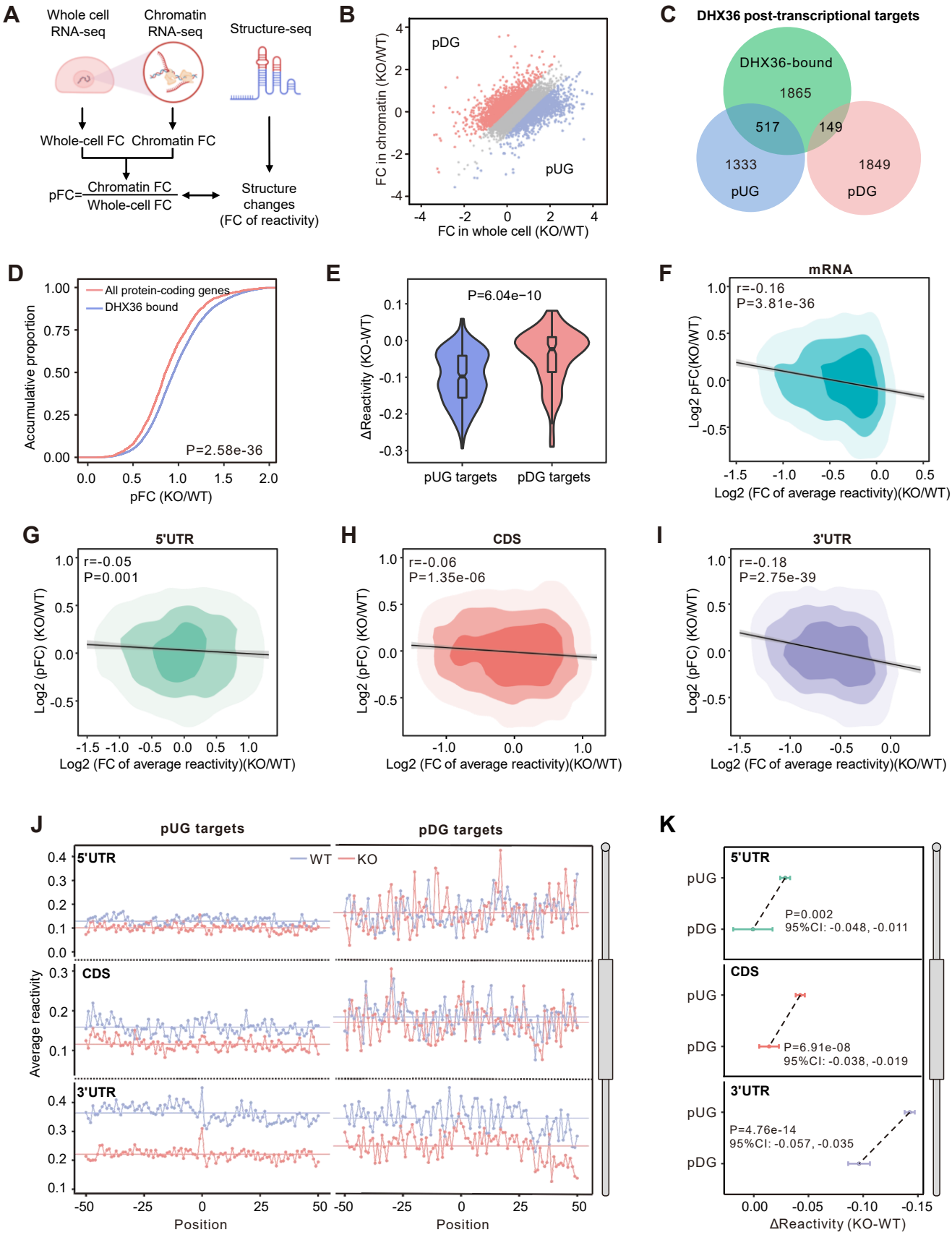

Zhang Y and Zhao J et. al. Figure 5

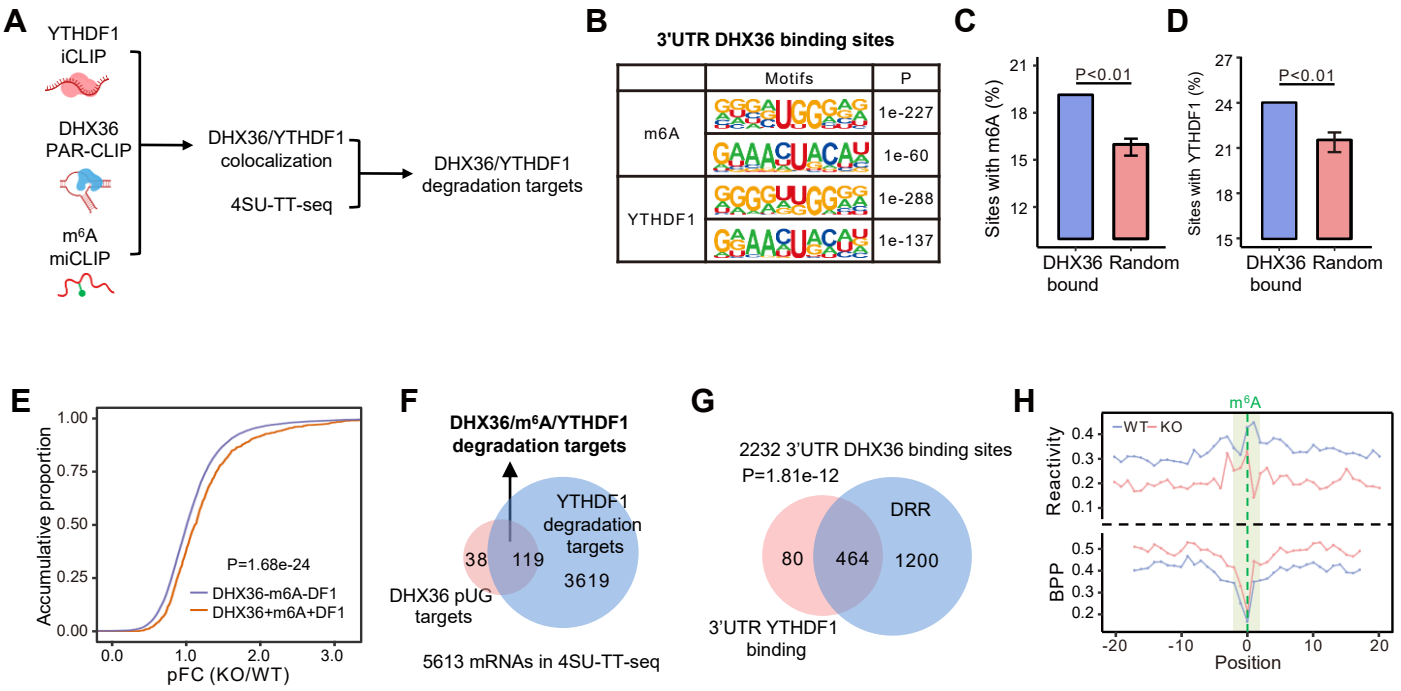

Zhang Y and Zhao J et. al. Figure 6

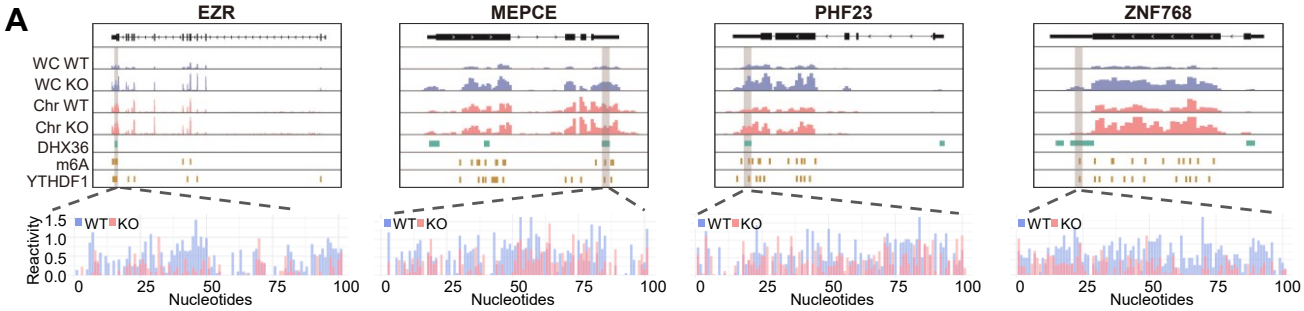

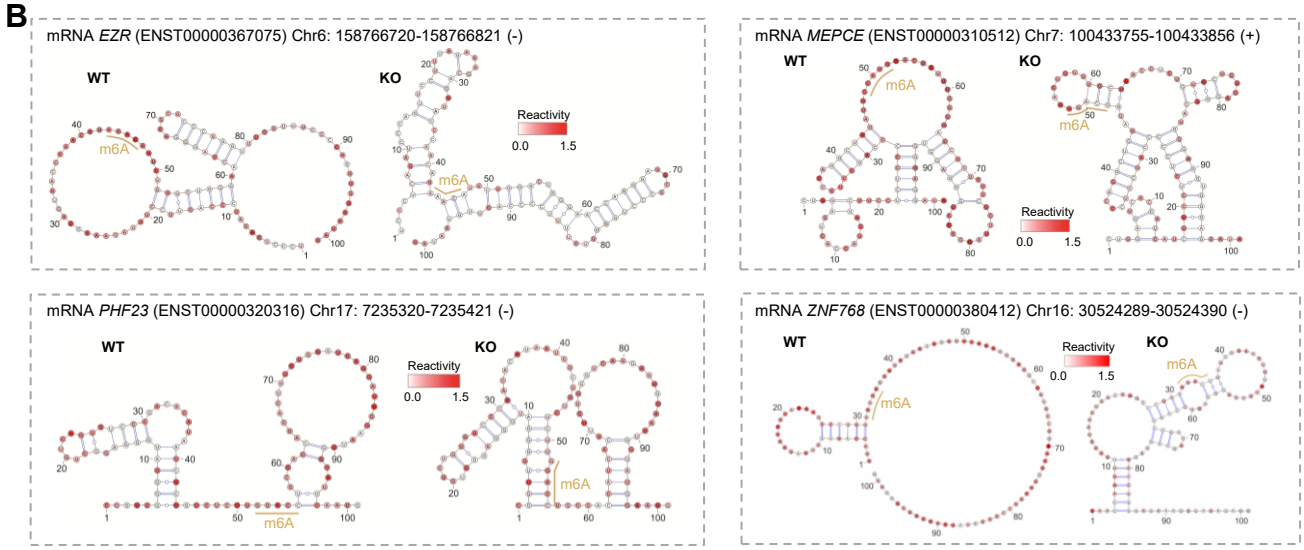

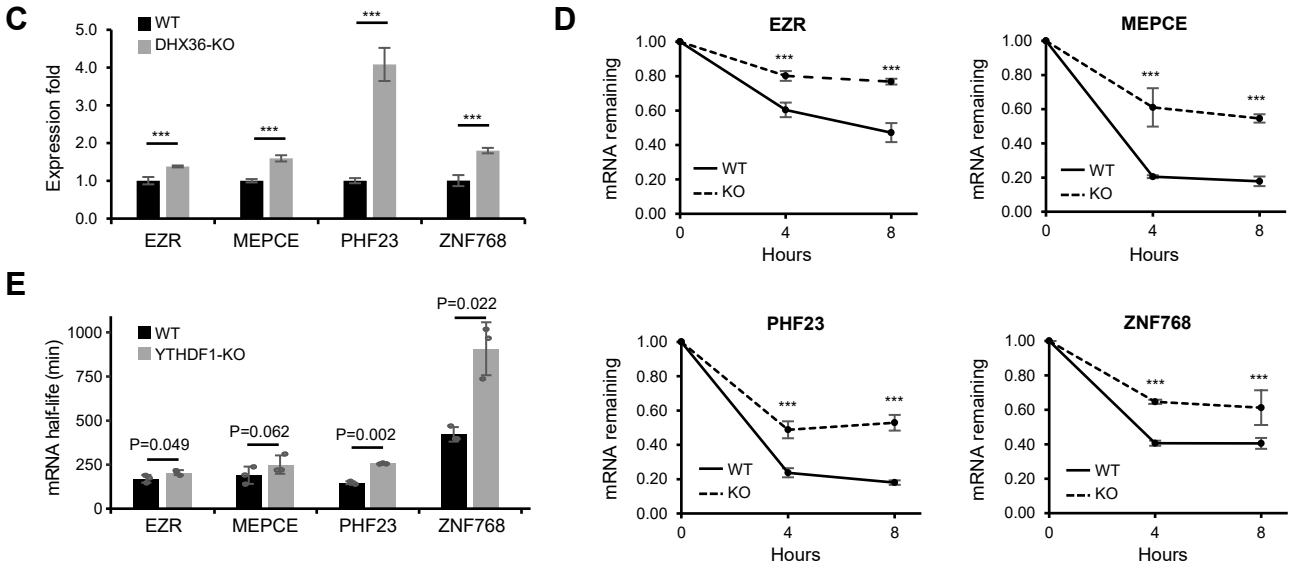

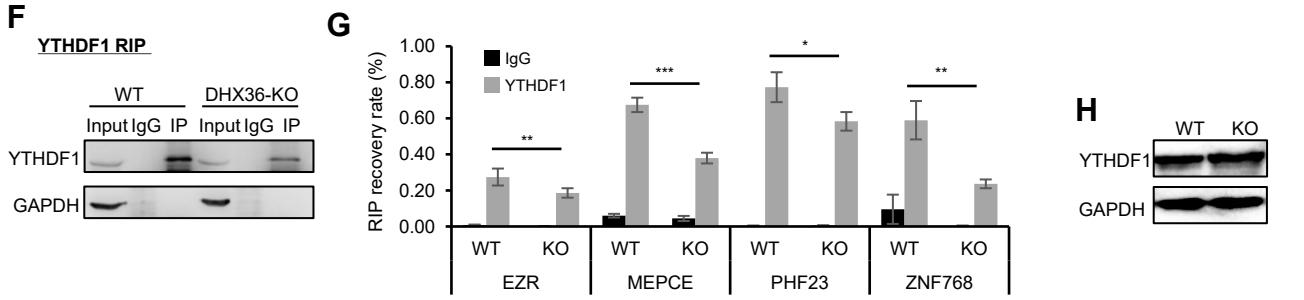
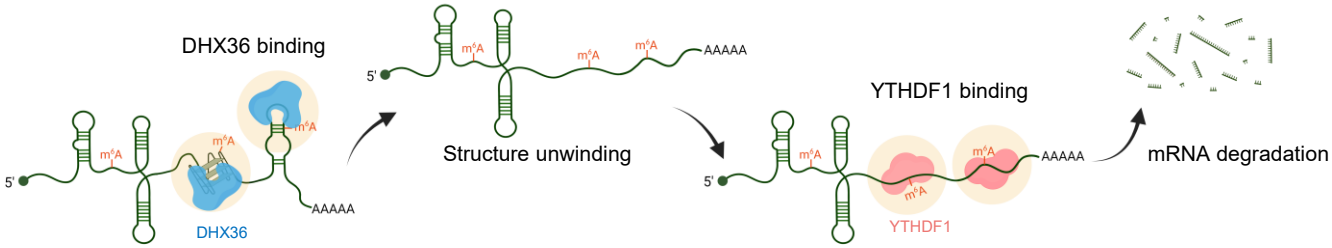
Zhang Y and Zhao J et. al. Figure 7